Turbulence and Stratification on the TOGA-COARE Microstructure Pilot Cruise

K. E. Brainerd and M. C. Gregg

Applied Physics Laboratory and School of Oceanography
College of Ocean and Fishery Sciences, University of Washington, Seattle

Abstract. On the TOGA-COARE pilot cruise, at 147°E, in the western Pacific warm pool, we profiled for seventeen days at 0°N, and for five days at 2°N. Winds were generally light, and variable in direction, but rainfall was often quite intense. Contrary to what is seen in the central equatorial Pacific, we did not observe a deep diurnal cycle in dissipation extending below the mixed layer. Strong daytime restratification often prevented nightly convective deepening down to the seasonal thermocline, resulting in surface forcing remaining trapped in a shallow layer. The relaxation of horizontal density gradients into vertical appears to be an important process driving restratification. Turbulent fluxes in the bottom of the mixed layer were generally small. Following rainfall, we observed pools of fresh water, that typically disappeared within a few hours, leaving the mixed layer nearly homogeneous in salinity; thus we did not observe a permanent barrier layer. Modeling such events using the Price-Weller-Pinkel model suggests a fresh pool will be mixed away on time scales of a few days, primarily by nighttime convection. The observed vetical structure can be accounted for by local vertical mixing processes.

1. Introduction

The warmest water in the world ocean is found in the western Pacific warm pool; this water, with sea surface temperature exceeding 27.5°C, drives intense convection in the atmosphere. This atmospheric convection is an important component of the equatorial Walker cell, of which the equatorial trade winds are one leg.

In ENSO years there is a cooling of the western equatorial Pacific surface waters, and warming in the central and eastern Pacific. The atmospheric convection follows the warm water eastward, resulting in major anomalies in the seasonal weather patterns through much of the global atmosphere. For example, Australia gets much less rain than in normal years, while the west coast of

DEPARTMENT OF THE NAVY
OFFICE OF NAVAL RESEARCH
SEATTLE REGIONAL OFFICE
1107 NE 45TH STREET, SUITE 350
SEATTLE WA 98105-4631

IN REPLY REFER TO:

4330
ONR 247
11 Jul 97

From: Director, Office of Naval Research, Seattle Regional Office, 1107 NE 45th St., Suite 350, Seattle, WA 98105
To: Defense Technical Center, Attn: P. Mawby, 8725 John J. Kingman Rd., Suite 0944, Ft. Belvoir, VA 22060-6218

Subj: RETURNED GRANTEE/CONTRACTOR TECHNICAL REPORTS

1. This confirms our conversations of 27 Feb 97 and 11 Jul 97. Enclosed are a number of technical reports which were returned to our agency for lack of clear distribution availability statement. This confirms that all reports are unclassified and are "APPROVED FOR PUBLIC RELEASE" with no restrictions.

2. Please contact me if you require additional information. My e-mail is *silverr@onr.navy.mil* and my phone is (206) 625-3196.

ROBERT J. SILVERMAN

Applied Physics Laboratory
College of Ocean and Fishery Sciences, University of Washington

30 May 1996

Scientific Officer
Code 322
Office of Naval Research
800 North Quincy Street
Arlington, VA 22217

To whom it may concern:

Please accept the enclosed articles, Turbulence produced by internal waves in the oceanic thermocline at mid and low latitudes" and "Turbulence and stratification on the TOGA-COARE microstructure pilot cruise," as the Final Technical Report for the project, Mixing Measurements for TOGA COARE, ONR grant #N00014-92-J-1419. This grant was in effect from 24 November 1992 through 31 March 1996.

Sincerely yours,

Michael C. Gregg
Principal Investigator

cc: ONR Resident Representative, University of Washington
Grant and Contract Services, University of Washington
Defense Technical Information Center ✓
Director, Naval Research Laboratory

1013 NE 40th Street Seattle, Washington 98105-6698 (206) 543-1300 FAX (206) 543-6785

REPORT DOCUMENTATION PAGE

Form Approved
OPM No. 0704-0188

1. AGENCY USE ONLY *(Leave blank)*	2. REPORT DATE	3. REPORT TYPE AND DATES COVERED
	Report Date	Technical

4. TITLE AND SUBTITLE
[1]Turbulence and stratificaton on the TOGA COARE microstructure pilot cruise and [2]Turbulence produced by internal waves in the oceanic thermocline at mid and low latitudes

5. FUNDING NUMBERS
N00014-92-J-1419

6. AUTHOR(S)
[1]K.E. Brainerd and M.C. Gregg
[2]M.C. Gregg, D.P. Winkel, T.B. Sanford and H. Peters

7. PERFORMING ORGANIZATION NAME(S) AND ADDRESS(ES)
Applied Physics Laboratory
University of Washington
1013 NE 40th Street
Seattle, WA 98105-6698

8. PERFORMING ORGANIZATION REPORT NUMBER
N/A

9. SPONSORING / MONITORING AGENCY NAME(S) AND ADDRESS(ES)
Office of Naval Research, Code 322
800 North Quincy Street
Arlington, VA 22217

10. SPONSORING / MONITORING AGENCY REPORT NUMBER
N/A

11. SUPPLEMENTARY NOTES

12a. DISTRIBUTION / AVAILABILITY STATEMENT
Distribution Statement

12b. DISTRIBUTION CODE

13. ABSTRACT *(Maximum 200 words)*

[1]This article is a report on the TOGA-COARE pilot cruise, at 147°E., in the Western Pacific warm pool, where profiling was accomplished for seventeen days at 0°N, and for five days at 2°N.

[2]When mid-latitude internal waves are at the background state modeled by Garrett and Munk, wave-wave interactons transfer energy to dissipative scales so slowly that instabilities generate overturns not much larger than the scales at which viscosity dissipates the turbulence. Consequently, high wavenumber spectra contain only the viscous decay portion of the universal turbulent spectrum.

14. SUBJECT TERMS
Subject Terms

15. NUMBER OF PAGES
Pages

16. PRICE CODE

17. SECURITY CLASSIFICATION OF REPORT	18. SECURITY CLASSIFICATION OF THIS PAGE	19. SECURITY CLASSIFICATION OF ABSTRACT	20. LIMITATION OF ABSTRACT
Unclassified	Unclassified	Unclassified	

South America gets far more.

Explanations for the causes of this eastward shift of the warm pool are still somewhat speculative, but one popular idea is that it is the result of Westerly bursts (periods of westerly winds blowing off the cold Asian continent in the northern winter). These typically consist of bursts of cold dry air, with velocities of $10\,\mathrm{m\ s^{-1}}$ or more, lasting a few days. These force a Yoshida jet, moving the warm surface waters to the east. Due to the impulsive nature of the forcing, they also generate Kelvin waves [*Lukas et al.*, 1984]; these result in a net movement of surface water to the east due to nonlinear interactions [*Harrison and Schopf*, 1984]. Thus there is a warming of surface waters in the equatorial central Pacific. The western Pacific is cooled largely due to increased latent heat flux [*Meyers et al.*, 1986]. Also, the movement of surface waters to the east results in a shallower thermocline, facilitating additional cooling by entrainment during subsequent westerly bursts. Thus, there is a cooling in the equatorial western Pacific, and the atmospheric convection center moves to the east.

Lukas [1987] has hypothesised that the occurrence of westerly bursts is promoted by elevated sea surface temperatures (SST) in the western warm-pool. Then the cooling of the western Pacific enables the resumption of easterlies and eventually the re-establishment of the western warm-pool.

The amount of heat supplied to the atmosphere here is quite sensitive to the temperature of the ocean surface, similar to the *Priestley* [1966] hypothesis, which suggests that the temperature of a moist surface in a warm climate is limited by latent heat flux. Small changes in SST cause variations in saturation vapor pressure at the surface, giving large changes in latent heat flux, J_L. For typical conditions, a change of 2°C in SST gives a change of about 100 $\mathrm{W\ m^{-2}}$ in J_L, which is quite significant. Thus, it seems that understanding the processes that control warm pool SST is vital in understanding the El Niño cycle.

Niiler and Stevenson [1982] have argued that in an equatorial warm pool bounded by an isotherm, the primary heat balance is between the surface heat flux and the turbulent heat flux out the bottom. *Lukas and Lindstrom* [1991] pointed out that the large excess of precipitation over evaporation in the Pacific warm pool leads to a shallow halocline embedded in a much deeper isothermal layer. The resulting shallow pycnocline inhibits the turbulent flux of heat; they hypothesized that the long-term heat balance was maintained by occasional deep entrainment events

associated with strong wind forcing. *Godfrey and Lindstrom* [1989] estimated turbulent heat fluxes out of the base of the mixed layer in this region based on measurements of the flux Richardson number (Ri_g) and the eddy diffusivity parameterization of *Pacanowski and Philander* [1981]. They concluded that typically this heat flux was very small, averaging 10 W m^{-2} or less, but that their observations did not rule out occasional energetic mixing events.

The Coupled Ocean-Atmosphere Response Experiment (COARE) microstructure pilot cruise was designed to provide estimation of fluxes from measurements of dissipation rates rather than inference from measurements of Ri_g, and to observe mixed layer response to wind and buoyancy forcing. We profiled at 147°E 0°N for 17 days (17 February to 6 March 1990, year days 48—65), then moved to 147°E 2°N for 4 days (6 March to 11 March, year days 65—70).

Our primary instrument for this study was the Advanced Microstructure Profiler (AMP), a free-falling instrument tethered to the ship by a fiber-optic cable that is kept slack during the drop, then used to recover the instrument. AMP measures temperature, conductivity, pressure, and microscale temperature gradients and velocity fluctuations. Fluctuations of horizontal velocities are measured by two airfoil lift probes capable of resolving shears from centimeter to meter scales [*Osborn and Crawford* 1980]. The rate of dissipation of turbulent kinetic energy, ϵ, is determined by integrating the shear spectra [*Shay and Gregg*, 1986], assuming that the turbulence is isotropic; i.e.,

$$\epsilon = 7.5\nu \int_{0.5\mathrm{cpm}}^{k_c} \phi_{\mathrm{shear}}(k)\, dk \quad [\,\mathrm{W\ kg^{-1}}\,] \tag{1}$$

where k_c is a variable cutoff wave number.

We made 3 to 4 drops per hour, totaling 1100 profiles on the equator and 275 at 2°N. At the equator we lost nearly a day of profiling due to the loss of an AMP (year day 52), and we halted AMP operations for 24 hours to allow optimal ship orientation for meteorological observations (year day 61). Drops were typically made from the weather side of the ship as it drifted with the wind abeam. Because each drop began in the wake of the ship (draft 4—5 m), dissipation rates from depths shallower than 0.05 MPa are not used. We do not know how deeply the ship's influence penetrates, so ϵ values from 0.05 to 0.15 MPa are considered suspect.

We obtained a continuous record of relative current profiles using an RD Instruments acoustic Doppler current profiler (ADCP), operating at 150 kHz, with a 4-m bin size. We have combined

these into hour-averages, giving an expected velocity uncertainty of 0.005 m s^{-1}.

Meteorological data was collected on the ship's SAIL loop, as well as by Chris Fairall and George Young, who mounted a 10-m mast on the ship's bow to support their instruments. From their data, they estimated surface fluxes by three methods: the bulk aerodynamic method, the direct covariance method, and the inertial-dissipation method [*Young et al.* 1992]. They were kind enough to supply us with their results; in general, we use their data in the analysis, rather than the SAIL loop data.

In this study we distinguish between mixed layers and mixing layers [*Brainerd and Gregg* 1995]. By mixed layer we mean the depth zone that has been mixed down from the surface within the relatively recent past; in this case it corresponds to the layer above the top of the seasonal thermocline. By mixing layer we mean the zone in which there is active turbulence being directly forced by surface fluxes; at night it is generally the zone in which convection is active, while during the daytime it is the zone in which wind and wave generated turbulence is active.

2. Observations

Meteorological Conditions

We went to the warm pool in the season when westerly bursts are most likely. The winter of 1990, however, was unusual; the Southern Oscillation Index (SOI) was dropping in January 1990 [*Climate Analysis Center* 1991], reaching in February its lowest point in 10 years (excluding El Niño years). Several strong westerly bursts, with wind speeds of 5 to 10 m s^{-1}, lasting 10—15 days, were observed in the western Pacific between November 1989 and January 1990 [*McPhaden et al.* 1992]. The sea surface west of 170°E cooled by as much as 0.5°C, while there was warming east of the dateline. West of the dateline there was an eastward jet in the upper 100 m, reaching velocities of 1 m s^{-1}, with a width of 400—600 km. Between the eastward surface jet and the undercurrent, there was a westward countercurrent, reaching velocities of 0.2—0.4 m s^{-1}.

Thus conditions appeared in many respects to match the start of an El Niño cycle. However, the center of atmospheric convection did not shift to the east, nor was there anomalous warming of the eastern Pacific warm tongue. By February, the SOI was returning towards zero, and the seemingly incipient El Niño fizzled out.

In our observations at 0°N, winds were generally very light, with occasional moderate wind events usually associated with squalls (Figure 1). The mean value of the wind work 10 m above the sea surface, $E_{10} = \tau U_{10}$, was 0.07 W m^{-2}, while the median value was 0.02 W m^{-2}. At 2°N the pattern in wind strength was similar, except for one day (year day 68) with $E_{10} \approx 2$—4 W m^{-2}. Winds alternated between being generally westerly and generally easterly. At 0°N, we observed 2 days of easterlies, then 5 days of westerlies, 6 days of easterlies, and 3 days of westerlies. At 2°N, winds were initially from the south, backing to north in the first 3 days; the day of strong winds started from the west and veered to the northeast in 18 hours. Fig. 1

We observed nearly 0.3 m of rainfall at 0°N, and about 0.02 m at 2°N; this corresponds to an excess of precipitation over evaporation of 0.24 m over the total observational period. The rain always corresponded to periods of westerly winds, and occurred as short intense bursts, typically lasting no more than 2 hours. The heaviest single rain brought nearly 0.1 m in 2 hours.

There was generally a regular alternation between surface heat fluxes giving warming during the day and cooling at night, with a total surface heat flux of $J_q^0 = -800$ W m^{-2} at noon on cloudless days and $J_q^0 = 100$—200 W m^{-2} at night. The heat loss went as high as 300 W m^{-2} during the windy night of day 68. The net long-wave radiation averaged nearly 60 W m^{-2} (upward), while the net short-wave radiation typically reached daily maxima of around -900 W m^{-2}. The average latent heat flux was about 80 W m^{-2}, and was strongly correlated with wind strength (correlation with wind stress 0.84), reaching maximum values exceeding 300 W m^{-2} during the strongest winds. Sensible and latent heat fluxes were strongly correlated with each other (correlation 0.85), but the sensible flux was an order of magnitude smaller. We have estimated the heat flux due to the temperature difference between falling raindrops and the sea surface by assuming the raindrops to be at the wetbulb temperature. (This may be an overestimate of their temperature, and hence an underestimate of the resulting heat flux, if the drops are not in thermal equilibrium with the surrounding atmosphere.) Calculated this way, the cruise-average heat flux due to raindrop temperature is 3.2 W m^{-2}; the average value during rainfall is 18.0 W m^{-2}. The maximum hourly average is more than 300 W m^{-2}; thus it is at times quite a large component of the total heat flux.

At the equator, J_q^0 is on average slightly positive (cooling) during the initial period of westerly winds, but is generally negative for the remainder of the equatorial station. At 2°N, the net trend

is warming, except during the high wind period, when increased latent and sensible heat fluxes give a net cooling trend. The station average values for J_q^0 are -56.9 W m^{-2} at 0°N, and 4.6 W m^{-2} at 2°N.

The diurnal pattern in J_b^0 is similar to J_q^0, except that rainfall causes negative spikes in J_b^0 (stabilizing), while it causes positive spikes in J_q^0 (cooling); thus it is clear that the rain's salinity flux had a stronger effect on buoyancy flux than did its heat flux.

Oceanographic Background

Historically, the western equatorial Pacific mixed layer was thought to be quite deep, as much as 100 m, largely due to the prevalence of temperature measurements and the dearth of salinity measurements. *Lukas and Lindstrom* [1991], using data from WEPOCS, pointed out that while there may be a deep isothermal layer, there is typically a halocline that is much shallower. Thus, the mixed layer depth must be determined from the depth of the pycnocline rather than the depth of the thermocline. The region west of the dateline has a large excess of precipitation over evaporation, while east of the date line there is a large excess of evaporation; the heat fluxes are nearly the same. Lukas and Lindstrom suggested that surface waters to the east, having substantially the same temperature as in the warm-pool but much higher salinity, are subducted under the fresher warm-pool waters, driven by prevailing easterly winds. Thus they attributed the observed structure of a deep isothermal layer, with a shallow halocline, to the difference in zonal length scales between surface freshwater and heat fluxes.

Our observations at the equator give station average profiles that are rather different from both the concepts described above, with a nearly-isothermal layer extending to 0.7 MPa, and a nearly-isohaline layer that is only slightly thinner, reaching to about 0.6 MPa (Figure 2). In the mean, we do not see a shallow isohaline layer embedded in a much deeper isothermal layer, nor do we see mixed layers as deep as 100 m. Both temperature and salinity in the mean have stable gradients in the mixed layer, with $\overline{N^2} \approx 3 \times 10^{-5}\,\mathrm{s}^{-2}$ (where the overbar denotes a station averaged value) in the upper 50 m (Figure 3, panel *a*). Stratification in this zone is dominated by salinity in the mean (Figure 3, panel *b*). The shallow salinity stratification in our mean profiles is due to the episodic presence of fresh pools associated with rain events; it appears to be the result of local processes rather than large-scale subduction, as will be discussed later. The absence of a permanent barrier

Fig. 2

Fig. 3

layer does not imply that salinity is unimportant to stratification, however. The mean profile of the stability ratio

$$R_\rho \equiv \frac{\alpha \partial T/\partial z}{\beta \partial s/\partial z} \tag{2}$$

shows that stratification is dominated by salinity throughout the upper water column, from the surface down to below the undercurrent core, except in the strongest part of the thermocline, from 0.7 to 1.2 MPa. Both temperature and salinity contribute to a rather strong pycnocline ($N^2 \approx 6 \times 10^{-4}\,\mathrm{s}^{-2}$) centered at 0.9 MPa, although it is dominated by temperature. Below that, stratification is nearly constant ($N^2 \approx 2 \times 10^{-4}\,\mathrm{s}^{-2}$) to 2.0 MPa. There is a broad, often double, salinity maximum between 1.2 and 2.1 MPa. and strong salinity variability in the core of the undercurrent (Figure 4), due to a series of salinity intrusions. Fig. 4

The record of θ at 0°N (Figure 5, panel *b*) begins with a warm shallow layer that deepens over the following six days, until the shallow thermocline merges with the seasonal thermocline. The salinity record for these days (panel *c*) shows evidence of strong advective effects. There is a salinity signature corresponding to the strong rain on day 49, but a much stronger salinity signal (fresh pool) on day 51, for which we observed almost no rain; lateral advection appears to be dominant for this day. Fig. 5

The mixed layer cooled between days 55 and 57, and warmed for the rest of the observations. During much of the period of easterly winds, with little rain, the mixed layer was nearly well-mixed in salinity down to 0.6—0.7 MPa. There was stronger salinity stratification the last few days of the observations, when we observed more rain.

At 2°N, the mixed layer was initially rather stratified in both θ and salinity (Figure 6), with a shallow mixing layer. The salinity record clearly shows strong advective effects, with multiple fresh pools, for some of which we observed no rainfall. The day of strong westerly wind homogenized the mixed layer in both θ and salinity to about 0.6 MPa, followed by the appearance of a cool fresh pool. Fig. 6

Profiles of daily averaged velocity at 0°N (Figure 7) show the core of the undercurrent near 1.6 MPa, and a maximum in the westward velocity at 0.8 MPa. Note the rather high shear above the westward velocity maximum and the wave-like structure in meridional velocity with vertical length scales of 50—70 m, giving significant shears. There is a maximum in meridional shear at the Fig. 7

depth of the undercurrent core that prevents a shear minimum at the zonal velocity maximum. At 2°N, the undercurrent is weaker, and the core is deeper (1.9 MPa), resulting in a weaker and more diffuse region of high zonal shear. Similar to the equatorial station, there is a wave-like structure in the meridional velocity, with vertical length scales of around 50 m.

Contours of shear squared, S^2, show considerable temporal variability at the equator (Figure 7). The high-shear zone heaves through a 10—20 m depth range semidiurnally for the first fortnight, sometimes with a corresponding cycle in magnitude. After day 58, the high-shear zone becomes weaker and more diffuse, as the westward maximum shallows and the undercurrent deepens and becomes slightly weaker. The patches of elevated S^2 below 1.3 MPa are mostly due to variability in the meridional velocity structure.

At 2 °N, the variation in S^2 at 0.7 MPa (Figure 8) is largely due to variability in meridional velocities; the elevated S^2 at this depth on day 69—69.5 appears to be related to the strong wind event. Elevated S^2 at 1.4 MPa is the result of coinciding maxima in shears of zonal and meridional velocities. Fig. 8

Profiles of gradient Richardson number calculated from cruise average profiles of N^2 and S^2 ($\widetilde{Ri_g} = \overline{N^2}/\overline{S^2}$) are rather different from both the Tropic Heat data from the central Equatorial Pacific [*Peters et al.*, 1988], and the western Equatorial Pacific data of *Godfrey and Lindstrom* [1989] (Figure 9). In Tropic Heat I, the case with the strong deep diurnal signal in dissipation, $\widetilde{Ri_g}$ was close to 0.25 down to about 0.8 MPa, then reached a very high maximum at the undercurrent core. Godfrey and Lindstrom at 150°E found $\widetilde{Ri_g} \approx 0.5$ down to 0.6 MPa, then two peaks of 8—12, at the South Equatorial Current and undercurrent maxima. In our equatorial data $\widetilde{Ri_g}$ was between 0.5 and 1.0 down to 0.6 MPa, then reached two peaks, both slightly more than 2, at the SEC and undercurrent maxima, with a minimum around 0.7 in the high shear zone above the core. Our data does not show a large $\widetilde{Ri_g}$ maximum at the undercurrent core, due to the presence of shear in meridional velocity corresponding to the depth at which zonal shear goes to zero. At 2°N, $\widetilde{Ri_g}$ was generally larger, due to the decreased shear. Nowhere in our profiles was $\widetilde{Ri_g} < 0.25$. Fig. 9

3. Turbulence

In this section we will consider the observed dissipation rates below the mixing layer, i.e. turbu-

lence not being directly driven by surface forcing, and we will attempt a parameterization based on Ri_g. Aside from the mixing layer, the most prominent feature of the dissipation record at 0°N is a band of high ϵ (10^{-8} — 3×10^{-7} W kg^{-1}) centered about 1.0 MPa, in the high zonal shear above the undercurrent core (Figure 10, panel *b*). There is a corresponding minimum in Ri_g (panel *a*), with minimum values of 0.25 — 0.75. But note that on days 62—64 the Ri_g minimum weakens and becomes somewhat deeper than 1.0 MPa; during the same period, the ϵ maximum shallows to about 0.85 MPa. It appears that the high dissipation is following the maximum in shear rather than the minimum in Ri_g (Figure 7). There is a patch of high dissipation (10^{-8} — 10^{-7} W kg^{-1}) at about 1.5 MPa starting on day 54 that loosely corresponds to low Ri_g (< 0.75) that is mostly the result of shear in meridional velocity; it is centered at the core of the undercurrent. Otherwise, dissipation below the high-shear zone is generally less than 10^{-8} W kg^{-1} . Above the high-shear zone, but below the mixing layer, there is elevated dissipation (5×10^{-9} — 10^{-7} W kg^{-1}) on days 48 — 51, giving a distinct subsurface local maximum; this is associated with a minimum in Ri_g (< 0.5). Fig. 10

At 2°N, Ri_g below the mixed layer shows a banded structure, alternating between about 1 and 10, with low Ri_g corresponding to depth ranges within which meridional and zonal shear combine to form shear squared maxima. There are corresponding maxima in dissipation, with ϵ reaching 5×10^{-8} W kg^{-1} at Ri_g minima, and dropping below 10^{-9} at Ri_g maxima.

In the central equatorial Pacific, it is common to find a deep diurnal cycle in dissipation, reaching much deeper than the diurnal mixing layer cycle in density. This has been attributed [*Peters et al.*, 1987] to internal waves forced by convective motions within the mixing layer, propagating downwards through the region of low Ri_g, where the added shear due to wave motions can be enough to cause a reduction of Ri_g below 0.25, leading to instabilities. This phenomenon is important, for the enhanced turbulent fluxes, and for the additional momentum flux accompanying the internal waves [*Wijesekera and Dillon*, 1991]. Our data shows no such deep cycle. A striking difference between the central Pacific data and our observations is that in the former, Ri_g just below the mixing layer is typically between 0.25 and 0.5; for our data it is typically between 0.5 and 1.

There is a significant difficulty in relating our observed dissipation rates to Ri_g, in that using the ADCP data we are unable to resolve shears on scales smaller than about 16 m. To effect a proper

parameterization of ϵ , we would need to estimate Ri_g on scales comparable to the overturning length scales of the turbulence; outside the mixed layer our observations show Thorpe scales that seldom exceed 5 m. Nevertheless, because many users of such parameterizations are large-scale modelers, whose models often cannot resolve shears smaller than 20 m, it may not be a useless exercise.

Perhaps the most widely used equatorial parameterizations are due to *Pacanowski and Philander* [1981], who parameterized the vertical eddy coefficient for momentum, K_m, and vertical eddy diffusivity, κ, as functions of Ri_g of the form:

$$K_m = \frac{\nu_0}{(1+\alpha Ri_g)^n} + \nu_b \tag{3}$$

$$\kappa = \frac{K_m}{(1+\alpha Ri_g)} + \kappa_b \tag{4}$$

They adjusted the constants in these relations in order to get realistic results from their equatorial model. *Peters et al.* [1988] used a similar form for K_ρ and K_h in the central equatorial Pacific. From cruise average profiles of density, velocity, and dissipation, they calculated Ri_g, $K_\rho = 0.2\epsilon/N^2$, and $K_h = 0.5\chi/(\partial\overline{T}/\partial z)^2$ (Figure 11). Averaging in depth bins, they found two branches; a shallow one (0.23—0.81 MPa, that included part of the mixed layer and the depth range of the deep diurnal signal in ϵ) with low Ri_g, where diffusivity increases very rapidly as Ri_g approaches 0.25 from above, and a deeper one (0.87—1.38 MPa). Compared with the relation found by *Pacanowski and Philander* [1981], the Tropic Heat diffusivities were almost an order of magnitude smaller for $Ri_g > 0.5$, but were higher for Ri_g near 0.25. Fig. 11

Our data, with both K_ρ and Ri_g calculated from hour-averages in 4-m bins, shows a very large scatter (Figure 11), with K_ρ ranging over 4-5 orders of magnitude for a given Ri_g. Estimating K_ρ and Ri_g from daily average profiles of ϵ , N^2, and S^2 does not collapse the data appreciably. A coherent pattern only emerges when cruise-averaged profiles are used; this gives a set of points falling between the Pacanowski and Philander and the Peters et al. lines, for depths exceeding 0.6 MPa, and a tail extending to higher K_ρ for shallower points. Fitting a line with the same form as used by *Peters et al.* [1988] to the points deeper than 0.6 MPa (Figure 11) gives

$$K_\rho = \frac{1.5\times10^{-3}}{(1+5Ri_g)^{2.5}} + 3\times10^{-6} \qquad \left[\mathrm{m^2 s^{-1}}\right] \tag{5}$$

It has been suggested by *Peters et al.* [1988] and by *Hebert et al.* [1991] that there may be a depth dependence to such a parameterization. Our deeper points are suggestive of such a dependence; the points are not just randomly scattered, but rather form definite loops. The size of the loops gives some indication of the magnitude of the depth dependence; they depart from the mean fit by factors of 2—3. For points shallower than 0.6 MPa, we believe that Ri_g is not a valid parameterization; this depth range includes the mixing layer, in which turbulence is being directly driven by surface forcing. Within the mixing layer it seems preferable to use a dissipation scaling based on that found by *Lombardo and Gregg* [1989] using the mid-latitude PATCHEX data:

$$\epsilon_s = 0.58 \left(\frac{J_b^0 + |J_b^0|}{2} \right) - 1.76 \frac{u_*^3}{\kappa z} \tag{6}$$

where ϵ_s is the scaled dissipation rate, $u_* = \sqrt{\tau/\rho}$, and κ is von Kármán's constant. Figure 12 is a plot of hour-averages in 0.5 m bins of $\psi = \epsilon/\epsilon_s$ against $\delta = -z/D$ where D is the mixing layer depth. Within the mixing layer, points are mostly centered around $\psi = 1$. There are some points where $\psi \gg 1$ that correspond to hours when $J_b^0 < 0$ and the wind is very light; i.e. when ϵ_s is close to zero. Beneath the mixing layer, where the diurnal thermocline provides isolation from surface forcing, ψ tends toward less than unity.

Fig. 12

4. Mixed and Mixing Layers

Restratification

In contrast to the central equatorial Pacific, where the mixing layer typically deepens to the seasonal thermocline every night, our observations show much variability in the nightly mixing layer deepening; only during a few nights does the mixing layer reach the seasonal thermocline. One reason for this variability is the strong restratification we observe in the mixed layer. In the case of weak restratification, convective deepening will extend to the thermocline nearly every night [*Lombardo and Gregg*, 1989], giving a more regular cycle. Thus we need to understand the processes that drive daily restratification in the mixed layer in order to understand the processes controlling the heat distribution and thus SST.

The COARE region differs from higher latitudes in several respects that may be important to restratification:

1. Insolation was particularly strong, with peak magnitudes of shortwave radiation exceeding 1000 W m^{-2}.

2. The water was exceptionally clear. Although we did not measure water clarity, we did observe that AMP was often visible to depths of 30 m or more. In comparison with a Secchi disk, with a diameter of 30 cm, the diameter of the AMP is only 16 cm. The depth at which the Secchi disk is visible varies linearly with diameter [*Preisendorfer*, 1986], giving an equivalent depth of 55 m for a 30 cm disk. In addition, the top of the AMP is not white, so the actual Secchi depth must have been greater than 55 m. Thus the water would have been clearer than Jerlov Type I.

3. Surface forcing was highly variable, on length scales of order 10 km. Rainfall in squalls was very intense, and often had length scales of only a few kilometers; surface buoyancy flux typically became strongly negative during squalls. Thus the surface forcing would tend to produce strong lateral density gradients.

In Figure 13 we show mean rates of growth of N^2 at 25 m, for all days on the equator for which the previous night's mixing layer deepened past 35 m. We compare this with the growth rate that would be expected due only to the local absorption of insolation (for Jerlov water type I), and that due to turbulent diffusion, based on observed dissipation rates, assuming eddy diffusivity for heat and salt is equal to the diffusivity for density $K_\rho = 0.2\epsilon/N^2$. Most of the increase in N^2 due to diffusivity occurs in the first hour, when turbulence from the previous night's convection is still strong; later, the contribution from diffusion is negligible. This is similar to what we observed in higher latitudes [*Brainerd and Gregg* 1993]. Most days show episodes of relatively strong stratification ($N^2 > 2 \times 10^{-5}$ s^{-2}), typically lasting a few hours. Neglecting the obvious episodic increases, there still appears to be a background rate of restratification in the remnant layer that exceeds the modeled restratification by roughly a factor of 2. Fig. 13

Note that for each day, N^2 is greater than zero at the start of restratification; this is consistent with the laboratory work of *Deardorff and Willis* [1982] and the subsequent analysis by *Mahrt and André* [1983], in which it was found that an active mixing layer is stratified in proportion to the ratio between the entrainment rate and the turbulence velocity u_*. They also concluded that stratification within the mixing layer is stronger near the bottom of the layer when the entrainment rate is small, approaching constant stratification through the mixing layer at high entrainment

velocities. Our data shows that for the last few hours of active convection, mean stratification is slightly negative ($\geq -1 \times 10^{-6}$ s^{-2}) in the upper half of the mixing layer, and is increasingly positive towards the bottom of the layer, reaching a maximum of $\approx 3 \times 10^{-6}$ s^{-2} (Figure 14). Fig. 14

We believe that one process contributing to the excess restratification beyond that due to insolation and vertical diffusion is the relaxation by advection of horizontal density gradients into vertical. The short length scale for variability in surface forcing due to squalls appears to be a source for such lateral density variations. We can do a simple scale analysis to investigate whether such a process will be of significance in our data set. Let us consider an idealized case, in which at the end of nighttime convection, the mixed layer is vertically well-mixed down to the seasonal pycnocline, but has a constant density gradient in the x direction. Because we were on the equator, we can use a very simple equation of motion:

$$\frac{\partial u}{\partial t} = \frac{1}{\rho_0}\frac{\partial p}{\partial x} \tag{7}$$

where x is distance in the direction of maximum density gradient, u is velocity in the x direction, ρ_0 is the mean density, and p is the pressure anomaly. For mixed layer depth D, the equation for the difference in velocity between the surface and the base of the mixed layer, $\mathcal{U}$, is

$$\frac{\partial \mathcal{U}}{\partial t} = \frac{Dg}{\rho_0}\frac{\partial \rho}{\partial x} \tag{8}$$

This leads to

$$\mathcal{U} = \frac{Dg}{\rho_0}\frac{\partial \rho}{\partial x}t \tag{9}$$

This is equivalent to the results of *Simpson and Linden* [1989] and *Tandon and Garrett* [1994], replacing f with βy, and letting $y \rightarrow 0$. Then

$$\mathcal{L} = \frac{Dg}{2\rho_0}\frac{\partial \rho}{\partial x}t^2 \tag{10}$$

where $\mathcal{L}$ is the horizontal distance between the intersections of an initially vertical isopycnal with the top and bottom of the mixed layer, and t is the time since the end of convective forcing. Then the stratification due to this process is

$$N^2 = \mathcal{L}\frac{\partial \rho}{\partial x}\frac{1}{D} = \frac{1}{2}\left(\frac{g}{\rho_0}\frac{\partial \rho}{\partial x}\right)^2 t^2 \tag{11}$$

This linearized solution will be applicable only if the scale of the lateral density variability, $\hat{L}$, is larger than $\mathcal{L}$.

We can estimate the scale of $\hat{L}$ from our AMP observations. Our measurements are some combination of a time series and a section; we remove much of the temporal variability by subtracting from the observed mixed layer density record the change in density corresponding to the integrated surface buoyancy flux, assuming it is trapped within the mixed layer (Figure 15). This will remove much of the variation on daily and longer time scales. We assume that the remaining variability (the difference between the thick and thin lines in Figure 15) is the lateral variation that we seek. We find the distance between AMP drops by integrating the relative velocity between the ship and the mixed layer, as measured by the ADCP. A spectrum of this density variability with respect to distance [*Press and Teukolsky*, 1988] rolls off at length scales less than 2—3 km, setting a lower bound for the length scale of $\hat{L}$. Differentiating the variability record with respect to distance gives a mean gradient $\overline{|\partial\rho/\partial x|} \approx 10^{-5}\mathrm{kg\,m^{-4}}$ (Of course we have no reason to think that the ship movements were in the direction of maximum density gradient, so this should be taken as a minimum value.) Using this value in (11), for $t = 6.75$ h, the mean duration of daytime negative surface buoyancy flux, gives a maximal restratification of $N^2 = 3 \times 10^{-6}$ s^{-2} between successive nightly convective mixing layer deepenings; this is similar in magnitude to the excess observed stratification. For the same time period, (10) gives a length scale for L of 1700 m; thus $\hat{L} > \mathcal{L}$, as required for the linearized solution to be valid.

Fig. 15

The observed length scales and magnitudes of density variability would give remnant layer restratification of sufficient magnitude to explain the observed growth in N^2, when combined with direct absorption of insolation and turbulent fluxes.

Effects of rainfall

Lukas and Lindstrom [1991] have hypothesized that the salinity barrier layer in the warm pool is the result of large scale processes, viz. subduction of high salinity water from the region of the dateline. Our observations suggest that the dominant processes are local. We observed a number of intense, localized rain events that left strong signatures in the upper ocean. Figure 16 shows a record for a typical such event; in this case we observed about 0.1 m of rain in 6 hours, the main rain event beginning shortly after the start of convective forcing in the early evening (panel *a*). We

Fig. 16

observe a pool of low-salinity water (panel *d*; salinity depressed by about 0.3 psu) that persists for a few hours and then disappears from our record. Because AMP profiles start at 4 m, it is possible that a shallower layer of fresh water remained undetected. However, because our measurements are made in the wake of the ship, we believe that the water column has been homogenized down to 6 or 8 meters depth by the presence of the ship. Thus we believe we would be able to detect the presence of a fresh layer, although we would not be able to observe its undisturbed vertical structure. We conclude that the fresh pool only lasts for a few hours before it is eliminated by some combination of vertical mixing and lateral advection (the ship has moved about 15 km relative to the mixed layer by the time the fresh pool completely disappears).

From our observations we cannot tell whether the fresh pool disappears due to mixing or simply because it advected away from our station, but from the total record of salinity at 0°N (Figure 5, panel *c*) it appears that the time scale over which such pools persist cannot be longer than a few days. During westerly winds, when most of the rainfall occurred (days 49—55, 62—65), we observed strong salinity stratification in the upper 20 m; during easterly winds, with weak rainfall, the mixed layer quickly becomes nearly well-mixed in salinity. During rainy periods we see mixed layer deepening inhibited by salinity stratification (e.g. days 51 and 62); during less rainy periods mixed layer dynamics appeared to be dominated by temperature.

In order to explore the net effect of rainfall in our data, we have made use of the Price Weller Pinkel mixed layer model (PWP). We modeled the processes at 0°N, using as initial conditions a nighttime profile during deep convection, and forcing it with the cruise-averaged daily meteorological cycle (with rainfall set to zero), letting the model run for 12 days. We made another run with identical initial conditions and the same surface forcing, with the addition of a 0.1-m rainfall early in the evening of the first day (corresponding to the heaviest single event that we observed). Figure 17 summarizes these runs. With no rain, the mixing layer deepens to 64 m during the first night's convection; this depth slowly increases on succeeding nights, reaching 68 m at the end of the run (panel *a*). In the case with the rain event, the mixing layer had reached 10 m when the rainfall occurred. Immediately after the rain, the depth decreased to 1 m, but mixing quickly broke through the shallow fresh pool, deepening to 18 m by the end of the first night. On following nights, mixing continued to deepen, reaching 50 m on the fifth night after the rain, reaching a near-equilibrium

Fig. 17

condition at 57 m depth by the tenth night. Both with and without the rain event, daytime mixing layer depths were only 1 m, as the mean wind was quite weak.

Plotting $\Delta SST = SST_{rain} - SST_{norain}$, where SST is taken to be the temperature in the top 1-m bin, we see an initial sharp drop in surface temperature due to the temperature of the falling raindrops (the surface heat flux due to the rain is 405 W m^{-2}), followed by elevated SST as the fresh water input inhibits convective deepening (panel *b*). The following day, SST remains depressed by 0.01 °C; afterwards inhibition of deepening results in elevated SST. Thereafter, ΔSST continues to rise at a decreasing rate, reaching a nearly constant value of about 0.025 °C after day 6.

Thus the net effect of the rain is to initially form a shallow pool of cold fresh water, that is quickly mixed downward by convection. In the next few days, convective deepening is slowed by the halocline left from the previous night's deepening (Figure 18); this gives a strong halocline embedded in a nearly isothermal profile, similar to the condition described by *Lukas and Lindstrom* [1991]. After 10—12 days, the final result is that convection nightly reaches a near-equilibrium depth that is about 10 m shallower than the no-rain case, with a correspondingly increased SST (Figure 18). In the final case, the halocline and thermocline coincide, unlike the condition described by *Lukas and Lindstrom* [1991]. Fig. 18

However, our observations suggest that rainfall occurs too frequently to allow an undisturbed evolution of a rain-formed layer over 12 days; thus we are led to examine the net effect of repeated rain episodes. Starting with the same initial conditions, we ran the model forced with the mean meteorological daily cycle, except with a 0.1-m rain event occurring every 5 days. The resulting mixing layer depths look much like the first 5 days of the single rain event run, repeating, except that there is a slight trend towards becoming shallower over the period of the run (Figure 19). Note that a random sampling of nightly mixing layer penetration from this run could give a record similar to the observations, with large day to day variability in the depth of convective deepening. The ΔSST record is also similar to the first 5 days of the previous run, repeated; i.e. it continues to increase at a rate of about 0.003 °C per day. It continues to warm as the mean surface heat flux is down; the major downward heat flux is due to shortwave insolation, which is mostly absorbed within the upper layers. The deeper convection of the no-rain run mixes this heat down through greater depths, resulting in a lower SST. Fig. 19

This process suggests that we should examine the sensitivity of the results to water clarity. The above runs were made assuming *Jerlov* [1968] Type I (upper 50 m) water, for which

$$I/I_0 = 0.68\exp(z/1.2) + 0.32\exp(z/28) \tag{12}$$

where z is the depth in meters, I is the irradiance at depth z, and I_0 is the irradiance that penetrates the surface. However, as mentioned above, we suspect that the water was actually of greater clarity during our observations. Thus we repeated the last PWP run using the relation suggested by *Krause* [1972] for very clear ocean water

$$I/I_0 = 0.4\exp(z/5) + 0.6\exp(z/40) \tag{13}$$

This gives rather different results (Figure 20). Because penetrating insolation is absorbed at much deeper depths, mixing layer depths are deeper. The no-rain depths are about 5 m deeper, while the rain-affected depths are about 20 m deeper than the Jerlov Type I cases (panel *a*). Because the mixing depths for the rain and no-rain cases are closer together, the rate of growth of ΔSST is much smaller for the run with clearer water. Fig. 20

Mixed Layer Heat Budget

Figure 21, panel *a*, shows a comparison between integrated surface heat and salt fluxes and heat storage at 0°N in a box whose bottom is defined by an isotherm in the upper part of the seasonal thermocline. Generally the heat storage term parallels the flux term, suggesting a simple local balance, with lateral advection and vertical fluxes out the bottom of the mixed layer being small, although there are occasional events, e.g. days 54—56, for which it appears that lateral advection is important. A local salinity balance is less successful (panel *b*). The integrated surface salt flux shows a series of rain events, separating periods of slight salinity increase due to evaporation; the net trend is freshening. The mixed layer salinity record shows short time scale variability with magnitudes similar to the integrated surface flux, but there is no general freshening trend. These short-period variations can be related to fresh pools seen in Figure 5; some of these correspond to rainfall that we observed, but many appear to have been formed by rain that fell elsewhere, creating squall wakes that advected past our station. Fig. 21

Godfrey and Lindstrom [1989], estimated the turbulent heat flux in the upper 100 m of the western equatorial Pacific to be less than 16 W m^{-2}, by combining measured Richardson numbers with

the Pacanowski and Philander parameterization. We are able to estimate eddy diffusivities from our turbulence measurements. Due to the presence of many salt-stabilized temperature inversions below the mixed layer, we do not use the heat diffusivity, estimated by the *Osborn and Cox* [1972] method. Assuming that $K_h \approx K_\rho = 0.2\epsilon/N^2$, and using the observed temperature profiles gives the turbulent heat flux J_q profiles shown in Figure 22. From the surface layer down to 0.8 MPa, these have magnitudes less than 10 W m^{-2} at both 0°and 2°N, consistent with the prediction of Godfrey and Lindstrom. Thus it appears that vertical fluxes driven by the mean shear are not very large; if they were the only process available to move heat out of the mixed layer, the long-term mean of the magnitude of J_q^0 could be no larger than 10 W m^{-2} in order to maintain a steady state temperature in the upper ocean. Fig. 22

However, estimating heat fluxes from dissipation rates ignores the effects of mixed layer dynamics; in particular it does not include fluxes due to convection, which within the mixing layer will be of much larger magnitude than the corresponding fluxes due to turbulent mixing (and opposite sign).

We believe we can identify at least one example of entrainment cooling due to deep mixing. On the night of day 58 we observed elevated wind strength with no accompanying rainfall to inhibit deepening (this is the only such event in our record); there is elevated ϵ extending from the surface down to the top of the seasonal thermocline (Figure 23). During this period there is active overturning at the base of the mixed layer (Figure 24). Corresponding to this period of deep mixing, there is a drop in mixed layer heat content of 2.3×10^7 J m^{-2} in 12 hours, a rate of about 520 W m^{-2} in excess of the surface heat loss, and an increase in salinity. This is suggestive of entrainment cooling, as the underlying water is colder and of higher salinity than the mixed layer. If we assume that the heat and salt fluxes across the base of the heat budget box are proportional to the temperature and salinity gradients, with equal eddy diffusivities, then we can predict the ratio of the rates of cooling and salinity increase from the observed gradients. Carrying out this estimate gives results within a factor of 2 of the observed rates. Thus we suggest that this appears to be an example of entrainment cooling of the mixed layer, although we must be cautious here, in view of the apparently advective variability seen throughout the record. Fig. 23

The rate of cooling observed during this one event removed the heat gained in about 5 days at

the station average surface heat flux. Thus, we conclude that mixed layer dynamics may be of first order importance to the heat budget, at least on time scales of several days or less; one must model the mixing layer well in order to model SST well. This presents a problem because of the extreme variability from day to day of our mixed layer observations. We believe much of this variability is due to the effects of squalls, which affect the mixed layer primarily through increased wind strength, increased latent heat flux, and by laying down a pool of cold fresh water. Not only do the squalls directly affect the mixed layer in their presence, but by leaving behind a wake of altered density structure, they can affect the mixed layer response long after the passing of the squall. For example, the fresh pool in a squall wake laid down in the morning may locally inhibit convective deepening the following night. We can see evidence of patchiness in mixed layer evolution in our record, where repositioning the ship a few kilometers results in a 20 or 30 m change in mixed layer depth. This patchiness strongly correlates with rainy conditions.

Effects of a Strong Wind Event

A canonical Westerly burst in this region would have wind speeds of 10 ms^{-1} or more, lasting for a week or two. Our observations do not include such an event; however, we did observe winds of that strength that persisted for one day, at 2°N. Because this is the major meteorological event in our record, we will examine the oceanic response in some detail.

The onset of the wind was quite sudden, with hour-average velocities rising from 2 to more than 12 m s^{-1} between 0600 and 0700 UTC on day 68, increasing to an hour-average peak of more than 16 m s^{-1} by 2200 UTC, then dropping back to 2 m s^{-1} by 0400 the next day. Initially from the west, the wind steadily veered around to come from the east by the time it died out. The period of strong wind corresponded to a period of positive J_b^0; enhanced latent and sensible heat fluxes during this time gave a total surface heat flux roughly twice that of the other nights observed at 2°N (400 W m^{-2} rather than 200 W m^{-2}).

In response to the strong surface forcing, the mixing layer deepened to almost 0.6 MPa, compared to the maximum depths of 0.3—0.4 MPa on the other nights at 2°N. In sharp contrast with the other nights here, where the Monin-Obukhov length, L, was much less than the mixing layer depth, D, on this night $0.5D < L < D$, suggesting that the wind was of importance comparable to free convection in driving the observed deepening of the mixing layer.

During this period of elevated wind strength, shear was small within the active mixing layer ($S^2 < 10^{-5}\,s^{-2}$), and increased at the base of the deepening mixing layer ($S^2 \approx 10^{-4}\,s^{-2}$). We observed an acceleration of the mixing layer that matched the direction of the surface stress down to a depth of at least 40 m. By the end of the wind event there was a patch of elevated shear (maximum $10^{-3}\,s^{-2}$), centered at 0.7 MPa at day 69.2, below the maximum depth of the mixing layer (Figure 25). This elevated shear persisted half a day after the wind; the resulting reduced Ri_g produced a patch of elevated dissipation ($10^{-8} < \epsilon < 10^{-6}$ W kg^{-1}) that persisted for 20 hours (Figure 25). Fig. 25

This patch of elevated turbulence, located at the top of the seasonal thermocline, might be expected to result in a significant turbulent heat flux out of the mixed layer. Comparing the heat content of the mixed layer with the integrated surface heat flux, we see that during the high winds and throughout the period when the patch of elevated turbulence persisted, the mixed layer lost heat at a rate of 500 W m^{-2}, or about 10 times the mean surface heat flux (Figure 26). Thus this appears to be a case of mixed layer cooling by entrainment. However, a similar comparison of mixed layer salt content with surface salt flux shows a rapid drop in salt content in the same period as the heat loss; because the salinity in the mixed layer is lower than that of the water just below, entrainment would act to increase mixed layer salinity. Thus we must conclude that lateral advection was dominant during this period. The salinity record shows a pool of cool fresh water appearing shortly after the end of the strong wind, although our observations showed no rainfall in the immediately preceding hours (Figure 6); this was presumably due to lateral advection, perhaps related to the strong wind. Fig. 26

5. Summary

Meteorological Conditions

1. At 0°N winds were mostly light, generally less than 5 m s^{-1}, with occasional events with winds approaching 10 m s^{-1}, associated with the passage of squalls. Wind direction was variable, with westerlies and easterlies alternating on time scales of several days.

2. At 2°N winds were also generally less than 5 m s^{-1}, with one 24-hour period of stronger winds, averaging 11 m s^{-1}, with peak hour-average exceeding 16 m s^{-1}. This event started as a

westerly, then steadily veered to become easterly.

3. We observed nearly 0.3 m of rain at 0°N, about 0.02 m at 2°N. Rain fell in intense bursts lasting typically 2-3 hours; the heaviest single event dropped nearly 0.1 m of rain in 2 hours. Rainfall was usually associated with periods of westerly winds.

4. The mean surface heat flux was -56.9 W m^{-2} (warming) at 0°N; and 4.6 W m^{-2} at 2°N.

Oceanic Conditions

1. At 0°N zonal currents show a westward maximum at about 0.8 MPa; the core of the undercurrent is at about 1.4 MPa; the difference in westward and eastward velocities is about 0.8 ms^{-1}. A wave-like structure in meridional velocity contributes significant shear, including a meridional shear maximum at the core of the undercurrent. At 2°N the zonal currents are weaker and the core of the undercurrent is deeper, giving weaker zonal shears. Waviness in meridional velocity results in significant shear.

2. In the mean, the nearly isohaline and nearly isothermal layers are of nearly the same depth; both salinity and temperature contribute to the mean stratification in the mixed layer.

Turbulence

1. Beneath the mixed layer, ϵ appears to be loosely related to Ri_g. Parameterization of ϵ by Ri_g using station-average values gives a line falling between the lines of *Pacanowski and Philander* [1981] and of *Peters et al.* [1988], with some evidence of depth dependence as well.

2. Within the mixing layer, observed ϵ agrees well with the *Lombardo and Gregg* [1989] scaling found on PATCHEX.

Restratification

1. Remnant layer restratification is stronger than seen in mid-latitudes on PATCHEX, resulting in the mixing layer often not deepening down to the seasonal thermocline during nighttime convection.

2. The strong restratification appears to be the result of strong insolation, clear water, and patchy surface forcing.

3. We believe direct absorption of insolation and relaxation of lateral density variability into stratification are important in driving remnant layer restratification. Turbulent fluxes are significant only in the first hour after the end of convective forcing.

Effects of Rainfall

1. Our observations show pools of fresh water following rainfall, that typically deepen and then disappear within a few hours. The mixed layer is nearly well-mixed in salinity much of the time between rain events.

2. Modeling a single rain event with the Price-Weller-Pinkel model suggests that nightly convection will deepen through a fresh pool in a few hours, but will take a few nights to reach a near-equilibrium depth. The final effect is to reduce the equilibrium depth by a few meters, raising SST by 0.03 °C.

Mixed Layer Heat Budget

1. Defining the bottom of the mixed layer by the depth of an isotherm in the top of the seasonal thermocline, we find that for much of the time a simple balance between surface heat flux and heat storage in the mixed layer appears to hold. Turbulent fluxes through the bottom of the mixed layer are usually quite small.

2. We also observed periods when the mixed layer heat budget appeared to be dominated by lateral advection, and identify one instance that appears to be entrainment cooling of the mixed layer at a rate exceeding 500 W m^{-2}.

6. Discussion

The patterns of turbulence and mixing that we observed in the western warm pool were quite different from those seen in the central equatorial Pacific. At 140°W, the mixing layer is typically observed to deepen to the top of the seasonal thermocline every night, and to be accompanied by a deep diurnal cycle in turbulence, characterized by elevated dissipation rates extending much deeper than the maximum mixing layer depth. In our data the depth of nighttime mixing layer deepening is quite variable from night to night, and there is no deep diurnal turbulence cycle.

We attribute the lack of a deep diurnal cycle to the higher Richardson number just below the mixing layer, compared with 140°W. In the central Pacific Ri_g is typically between 0.25 and 0.5, whereas in our data it is typically between 0.5 and 1. Presumably this difference is due to the difference in surface forcings; in the central Pacific the trade winds are strong and steady, while in our observations winds were weak and variable in direction, and thus unable to maintain a strong shear field. Also, the equatorial undercurrent is weaker and deeper in the western Pacific.

We attribute the large day-to-day variability in mixed layer depth in our data to strong variability in surface forcing due to squalls, and to strong remnant layer restratification. Where restratification is weak, nighttime convection will deepen to the top of the seasonal thermocline each night, giving a regular daily cycle. Where restratification is strong, the penetration depth of convection is sensitive to details of surface forcing and to the history of mixing of the water column.

We can identify several causes for unusually strong restratification in the western warm pool. Firstly, because of the low latitude, insolation was quite strong, with shortwave radiation exceeding 1000 W m^{-2}. Because the water was exceptionally clear, more radiation penetrates through the surface layer to stratify the remnant layer through direct absorption at depth. It also appears that strong variability in surface forcing on length scales of a few kilometers due to squalls contributes significantly to restratification through the relaxation of lateral density variations into stratification.

The significant result of strong restratification of the remnant layer is that by inhibiting the nighttime mixing layer from deepening to the seasonal thermocline, surface forcing remains trapped within a shallow surface layer. In particular, the net surface flux of heat during our observations was into the ocean. Thus the net effect of strong restratification would be to raise the temperature of the surface layer, strengthening the stratification, and forming a positive feedback loop.

It is clear that correctly modeling the restratification in the remnant layer is important if one is correctly to model SST, at least on time scales of a few days or less. Our results suggest this may be difficult to do with a conventional one-dimensional mixed layer model. Lateral processes appear to be important, and would of course require a multi-dimensional model. Further, our modeling results are quite sensitive to the optical properties of the water column. Although the water remained very clear during our observations, *Siegel et al.* [1995], during the TOGA-COARE IOP, observed strong variability in optical properties due to a phytoplankton bloom resulting from a deep mixing event that brought nutrients up into the surface layer. Thus it would seem that a combined biological-physical model may be required in order to model SST accurately.

Rainfall in our observations was often very intense, and very localized in space and time, occurring in squalls with length scales of a few kilometers and time scales of a few hours; we observed as much as 0.1 m of rain in two hours. Following heavy rains, our observations show fresh pools, that typically deepen and then disappear within a few hours. The mixed layer is nearly well-mixed in

salinity much of the time between rain events. Modeling a single rain event using the Price-Weller-Pinkel model suggests that nightly convection will deepen through a fresh pool in a few hours, but will take a few nights to reach a near-equilibrium depth.

Lukas and Lindstrom [1991] suggested that the typical state of the Western warm pool is a shallow halocline embedded in a much deeper isothermal layer, the shallow halocline defining the bottom of a barrier layer that would inhibit entrainment cooling of the surface layer. Thus heat added at the surface would be trapped within the barrier layer, except for occasional deep mixing driven by strong winds. They hypothesized that this is the result of subduction of warm salty water from east of the date line under warm fresher water resulting from heavy precipitation within the warm pool. We do not see a permanent barrier layer, and do not need to invoke subduction to explain our observations. However, the net effect of excess precipitation is to decrease salinity in the mixed layer, resulting in a stronger halocline at the base of the mixed layer, which does inhibit entrainment cooling.

Defining the bottom of the mixed layer by the depth of an isotherm in the top of the seasonal thermocline, we find that for much of the time a simple balance between surface heat flux and heat storage in the mixed layer appears to hold. This suggests that turbulent fluxes through the bottom of the mixed layer are small most of the time; our estimates based on the dissipation rate are typically found to be small. We also observed periods when the mixed layer heat budget appeared to be dominated by lateral advection, and identify one instance that appears to be entrainment cooling of the mixed layer at a rate exceeding 500 W m^{-2}.

Acknowledgments. The Office of Naval Research funded collection of these data. The analysis was supported by the "Mixing to Mesoscale" University Research Initiative. One author (KB) was supported by an Office of Naval Research fellowship for part of this work. The authors thank Ren-Chieh Lien, Hemantha Wijesekera, Harvey Seim, and David Winkel for many helpful comments and discussions, and Chris Farrell for the use of his meteorological data. Captain Doyle and the crew of the R/V Wecoma were extremely helpful throughout the cruise. Contribution xxxx of the School of Oceanography, University of Washington.

List of References

Brainerd, K. E., and M. C. Gregg, Diurnal restratification and turbulence in ht eoceanic surface mixed layer 2. Modeling, *J. Geophys. Res., 98*, 22,657–22,664, 1993.

Brainerd, K. E., and M. C. Gregg, Surface mixed and mixing layer depths, *Deep Sea Res., 42*, 1521–1543, 1995.

Climate Analysis Center, Climate diagnostics bulletin, Near real-time analyses, January 1991, 63 pp., Natl. Oceanic and Atmos. Admin., U.S. Dep. of Commer., Washington D.C., 1991.

Deardorff, J. W., and G. E. Willis, Dependence of mixed-layer entrainment on shear stress and velocity jump, *J. Fluid Mech., 115*, 123–149, 1982.

Godfrey, J. S., and E. J. Lindstrom, The heat budget of the equatorial western Pacific surface mixed-layer, *J. Geophys. Res., 94*, 8007–8017, 1989.

Harrison, D. E. and P. S. Schopf, Kelvin wave-induced anomalous advection and the onset of surface warming in El Niño events. *Mon. Wea. Rev., 112*, 923–933, 1984.

Hebert, D., J. N. Moum, and D. R. Caldwell, Does oceanic turbulence peak at the equator?: Revisited, *J. Phys. Oceanogr*, 1690–1698, 1991.

Jerlov, N. G., *Optical Oceanography*, Elsevier, 194 pp., 1968.

Krause, E. B., *Atmosphere-Ocean Interaction.* Oxford University Press, 275 pp., 1972.

Lombardo, C. P., and M. C. Gregg, Similarity scaling during nighttime convection, *J. Geophys. Res., 94*, 6273–6284, 1989.

Lukas, R., On the role of western Pacific air-sea interaction in the El Niño / Southern Oscillation phenomenon, **Proceedings of the U.S. TOGA Western Pacific Air-Sea Interaction Workshop**, R. Lukas and P. Webster, eds, Honolulu, 1987.

Lukas, R., and E. Lindstrom, The mixed layer of the western equatorial Pacific Ocean, *J. Geophys. Res., 96*, 3343–3357, 1991.

Lukas, R., S. P. Hayes, and K. Wyrtki, Equatorial sea level response during the 1982–1983 El Niño , *J. Geophys. Res., 89*, 10,425–10,430, 1984.

Mahrt, L, and J.-C. André, On the stratification of turbulent mixed layers, *J. Geophys. Res., 88*, 2662–2666, 1983.

McPhaden, M. J., F. Bahr, Y. du Penhoat, E. Firing, S. P. Hayes, P. P. Niiler, P.L. Richardson, and J.M. Toole, The response of the western equatorial Pacific Ocean to westerly wind bursts during November 1989 to January 1990, *J. Geophys. Res., 97*, 14,289–14,303, 1992.

Meyers, G., J. R. Donguy, R. K. Reed, Evaporative cooling of the western equatorial Pacific Ocean by anomalous winds, *Nature, 323*, 523–526, 1986.

Niiler, P. and J. Stevenson, The heat budget of tropical ocean warm-water pools, *J. Marine Res., 40 (Suppl)*, 465–480, 1982.

Osborn, T. R., and C. S. Cox, Oceanic fine structure, *Geophys. Fluid Dyn., 3*, 321–345, 1972.

Pacanowski, R. C., and S. G. H. Philander, Parameterization of vertical mixing in numerical models of tropical oceans, *J. Phys. Oceanogr., 11*, 1443–1451, 1981.

Peters, H., M. C. Gregg, D. R. Caldwell, and J. N. Moum, Equatorial vertical mixing. In **Further Progress in Equatorial Oceanography: A Report of the U.S. Workshop on the Dynamics of the Equatorial Oceans, Honolulu, Hawaii, August 11–15 1986**, E. Katz and J. Witte, eds., Ft.Lauderdale, 1987.

Peters, H., M. C. Gregg, J. M. Toole, On the parameterization of equatorial turbulence, *J. Geophys. Res., 93*, 1199–1218, 1988.

Preisendorfer, R. W., Secchi disk science: Visual optics of natural waters, *Limnol. Oceanogr., 31*, 909–926, 1986.

Press, W. H., and S. A. Teukolsky, Search algorithm for weak periodic signals in unevenly spaced data, *Computers in Physics, 2*, 77–80, 1988.

Priestley, C. H. B., The limitation of temperature by evaporation in hot climates, *Agricultural Meteorology, 3*, 241–246, 1966.

Siegel, D. A., J. C. Ohlmann, L. Washburn, R. R. Bidigare, C. T. Nosse, E. Fields, and Y. Zhou, Solar radiation, phytoplankton pigments and the radient heating of the equatorial Pacific warm pool, *J. Geophys. Res., 100*, 4885–4891, 1995.

Simpson, J. E., and P. F. Linden, Frontogenesis in a fluid with horizontal density gradients, J. Fluid Mech., 202, 1–16, 1989.

Tandon, A., and C. Garrett, Mixed layer restratification due to a horizontal density gradient, *J. Phys. Oceanogr., 24*, 1419–1424, 1994.

Wijesekera, H. W. and T. M. Dillon, Internal waves and mixing in the upper equatorial Pacific Ocean, *J. Geophys. Res., 96*, 7115–7125, 1991.

Young, G. S., D. V. Ledvina, and C. W. Fairall, Influence of precipitating convection on the surface energy budget observed during a tropical ocean global atmosphere pilot cruise in the tropical western Pacific Ocean, *J. Geophys. Res., 97*, 9595–9603, 1992.

CAPTIONS

Figure 1 Meteorological observations.

Panel *a*. $E_{10} \equiv \tau U_{10}$.

Panel *b*. Wind direction (shaded) and integrated rainfall.

Panel *c*. Sea surface temperature (heavy line) and air temperature (thin line).

Panel *d*. Surface heat flux J_q^0 (thin line, shaded) and its time integral (heavy line).

Figure 2 Station-average profiles at 0°N (panel *a*) and 2°N (panel *b*).

Figure 3 Station-average stratification.

Panel *a*. Mean N^2 at 0°N.

Panel *b*. Median R_ρ at 0°N.

Panel *c*. Mean N^2 at 2°N.

Panel *d*. Median R_ρ at 2°N.

Figure 4 Theta-salinity diagrams for 0°N (panel *a*) and 2°N (panel *b*). Note signature of multiple intrusions at 0°N, which are near the core of the undercurrent.

Figure 5 Contours of θ and salinity at 0°N.

Panel *a*. Surface buoyancy flux J_b^0 (light shading) and rainfall rate (dark shading).

Panel *b*. Contours of θ, hour-averages in 4-m bins. Thin lines are contours of θ at 1°C intervals. Thick line is mixing layer depth.

Panel *c*. Contours of salinity, hour-averages in 4-m bins. Thin lines are contours of salinity at 0.2 psu intervals. Thick line is mixing layer depth.

Figure 6 Contours of θ and salinity at 2°N.

Panel *a*. Surface buoyancy flux J_b^0 (light shading) and rainfall rate (dark shading).

Panel *b*. Contours of θ, hour-averages in 4-m bins. Thin lines are contours of θ at 0.5°C intervals. Thick line is mixing layer depth.

Panel *c*. Contours of salinity, hour-averages in 4-m bins. Thin lines are contours of salinity at 0.2 psu intervals. Thick line is mixing layer depth.

Figure 7 Shear squared at 0°N.

Panel *a*. Contours of hour-averages of shear squared S^2 at 0°N, from ADCP data. Vertical resolution is about 16 m. Thin line is mixing layer depth. Thick line is the depth of the core of the

undercurrent.

Panel *b*. Profiles of 24-hour averages of zonal (solid lines) and meridional (dashed lines) velocities.

Figure 8 Shear squared at 2°N.

Panel *a*. Contours of hour-averages of shear squared S^2 at 2°N, from ADCP data. Vertical resolution is about 16 m. Thin line is mixing layer depth. Thick line is the depth of the core of the undercurrent.

Panel *b*. Profiles of 24-hour averages of zonal (solid lines) and meridional (dashed lines) velocities.

Figure 9 Station-averaged profiles.

Panel *a*. $\overline{N^2}$ (shaded) and $\overline{S^2}$ at 2°N.

Panel *b*. Gradient Richardson number Ri_g at 2°N.

Panel *c*. ϵ at 2°N.

Panel *d*. $\overline{N^2}$ (shaded) and $\overline{S^2}$ at 0°N.

Panel *e*. Gradient Richardson number Ri_g at 0°N.

Panel *f*. ϵ at 0°N.

Figure 10 Richardson number and dissipation at 0°N.

Panel *a*. Gradient Richardson number Ri_g, calculated at about 16-m resolution, in hour-averages.

Panel *b*. Dissipation rate ϵ, hour averages in 5-m bins.

Figure 11 Parameterizing K_ρ with Ri_g. Each small dot is an hour-averaged 4-m bin (starting at 0.17 MPa) of Ri_g and $K_\rho = 0.2\epsilon/N^2$ (vertical resolution about 16 m). The lines with large symbols are formed by calculating Ri_g and K_ρ from cruise-averages of ϵ, S^2, and N^2. The line with open symbols is for data 0.57 MPa and shallower, the line with closed symbols is for 0.61 MPa and deeper. The dashed line is the Pacanowski and Philander parameterization; the dot-dashed line is the Peters et al. parameterization.

Figure 12 Dissipation in mixing layer parameterized by surface forcing. Each point is an hour-average of $\psi = \epsilon/\epsilon_s$ (where ϵ_s is the mixing layer scaling of *Lombardo and Gregg* [1989]) against $\delta = -z/D$ where D is the mixing layer depth.

Figure 13 Restratification within the remnant layer. Each thin solid line is the observed N^2 at 0.25 MPa for the labeled year day. The heavy dashed line is the growth in stratification at 0.25 MPa that would be expected due only to direct absorption of insolation at depth, averaged over the days

shown. The heavy solid line (with 95% confidence interval shaded) is the growth of stratification at 0.25 MPa that would be expected due to insolation and turbulent buoyancy flux estimated from observed dissipation, assuming $J_b = 0.2\epsilon$.

Figure 14 Profile of N^2 plotted against $\delta = -z/D$, averaged over hours of active convection. Stratification is slightly negative in the upper half of the mixing layer, becoming increasingly positive in the lower half. Shading shows 95% confidence intervals.

Figure 15 Time series of integrated J_b^0 (expressed as mass flux; heavy line), compared with observed variability of mass in the mixed layer (mean density above an isotherm in the top of the seasonal thermocline, multiplied by mean depth of the thermocline; thin line with + symbols).

Figure 16 Record of a strong rain event, during which almost 0.1 m of rain was observed.

Panel *a*. Rainfall rate (light shading) and surface buoyancy flux J_b^0 (dark shading; the negative extremum reaches -3.5×10^{-6} W kg^{-1}).

Panel *b*. Contours of hour-averages of ϵ in 1-m bins; contoured by decades.

Panel *c*. Contours of θ averaged in 1-m bins; contour interval 0.1°C.

Panel *d*. Contours of salinity averaged in 1-m bins; contour interval 0.05 psu. The fresh pool formed by heavy rainfall has completely disappeared within 8 hours.

Figure 17 PWP output for a single rain event.

Panel *a*. Mixing layer depth, comparing results for forcing with no rain (shading) with results for 0.1 m of rain (heavy line).

Panel *b*. Difference in temperature in top 1 m bin, $\Delta\mathrm{SST} = \mathrm{SST}_{\mathrm{rain}} - \mathrm{SST}_{\mathrm{norain}}$.

Figure 18 PWP output.

Panel *a*. Profiles of θ on day 1 of simulation, with 0.1 m rain (solid line) and with no rain (dashed line).

Panel *b*. Profiles of salinity on day 1 of simulation, with 0.1 m rain (solid line) and with no rain (dashed line).

Panel *c*. Profiles of θ on day 10 of simulation, with 0.1 m rain (solid line) and with no rain (dashed line).

Panel *d*. Profiles of salinity on day 10 of simulation, with 0.1 m rain (solid line) and with no rain (dashed line).

Figure 19 PWP output: for repeated rainfall (0.1 m rain every 5 days), Jerlov Type I water.

Panel *a*. Mixing layer depth, comparing results for forcing with no rain (shading) with results for 0.1 m of rain (heavy line).

Panel *b*. Difference in temperature in top 1 m bin, $\Delta\mathrm{SST} = \mathrm{SST}_{\mathrm{rain}} - \mathrm{SST}_{\mathrm{norain}}$.

Figure 20 PWP output: for repeated rainfall (0.1 m rain every 5 days), for very clear water.

Panel *a*. Mixing layer depth, comparing results for forcing with no rain (shading) with results for 0.1 m of rain (heavy line).

Panel *b*. Difference in temperature in top 1 m bin, $\Delta\mathrm{SST} = \mathrm{SST}_{\mathrm{rain}} - \mathrm{SST}_{\mathrm{norain}}$.

Figure 21 Mixed layer budgets at 0°N.

Panel *a*. Heat budget within the mixed layer at 0°N. Integrated surface heat flux (shaded) and heat content down to the 28.66°C isotherm, in the top of the thermocline.

Panel *b*. Salt budget within the mixed layer at 0°N. Integrated surface salt flux (shaded) and salt content down to the 28.66°C isotherm.

Figure 22 Turbulent heat fluxes inferred from dissipation measurements.

Panel *a*. Station averages of eddy diffusivity, $K_\rho = 0.2\epsilon/N^2$.

Panel *b*. Station averages of turbulent heat fluxes, estimated assuming $K_\mathrm{h} \approx K_\rho$.

Panel *d*. Station averages of θ.

Figure 23 Turbulence summary at 0°N.

Panel *a*. Surface buoyancy flux (red shading) and E_{10} (green shading).

Panel *b*. Contours of hour-averages of ϵ; heavy black line is mixing layer depth; square symbols are Monin-Obukhov length; thin lines are isotherms.

Figure 24 Profiles of σ_θ (heavy line) and ϵ (shaded) during deep entrainment. Elevated dissipation extends down to the top of the thermocline, and overturns are evident at the base of the mixed layer.

Figure 25

Strong wind event at 2°N.

Panel *a*. Surface buoyancy flux J_b^0 (dark shading) and E_{10} (light shading).

Panel *b*. Contours of shear squared (about 16-m resolution) during the strong wind event. Note elevated shear at about 0.7 MPa following the period of strong wind; slightly elevated shear at base

of mixing layer during wind, weak shear in interior of mixing layer.

Panel *c*. Gradient Richardson number Ri_g, calculated at about 16-m resolution, in hour-averages; not reduced Ri_gat base of mixed layer following strong wind.

Panel *d*. Dissipation rate ϵ, hour averages in 5-m bins, showing elevated dissipation persisting at base of mixed layer following strong wind.

Figure 26 Mixed layer budgets at 2°N.

Panel *a*. Heat budget within the mixed layer at 2°N. Integrated surface heat flux (shaded) and heat content down to the 29.05°C isotherm, in the top of the thermocline.

Panel *b*. Salt budget within the mixed layer at 2°N. Integrated surface salt flux (shaded) and salt content down to the 29.05°C isotherm.

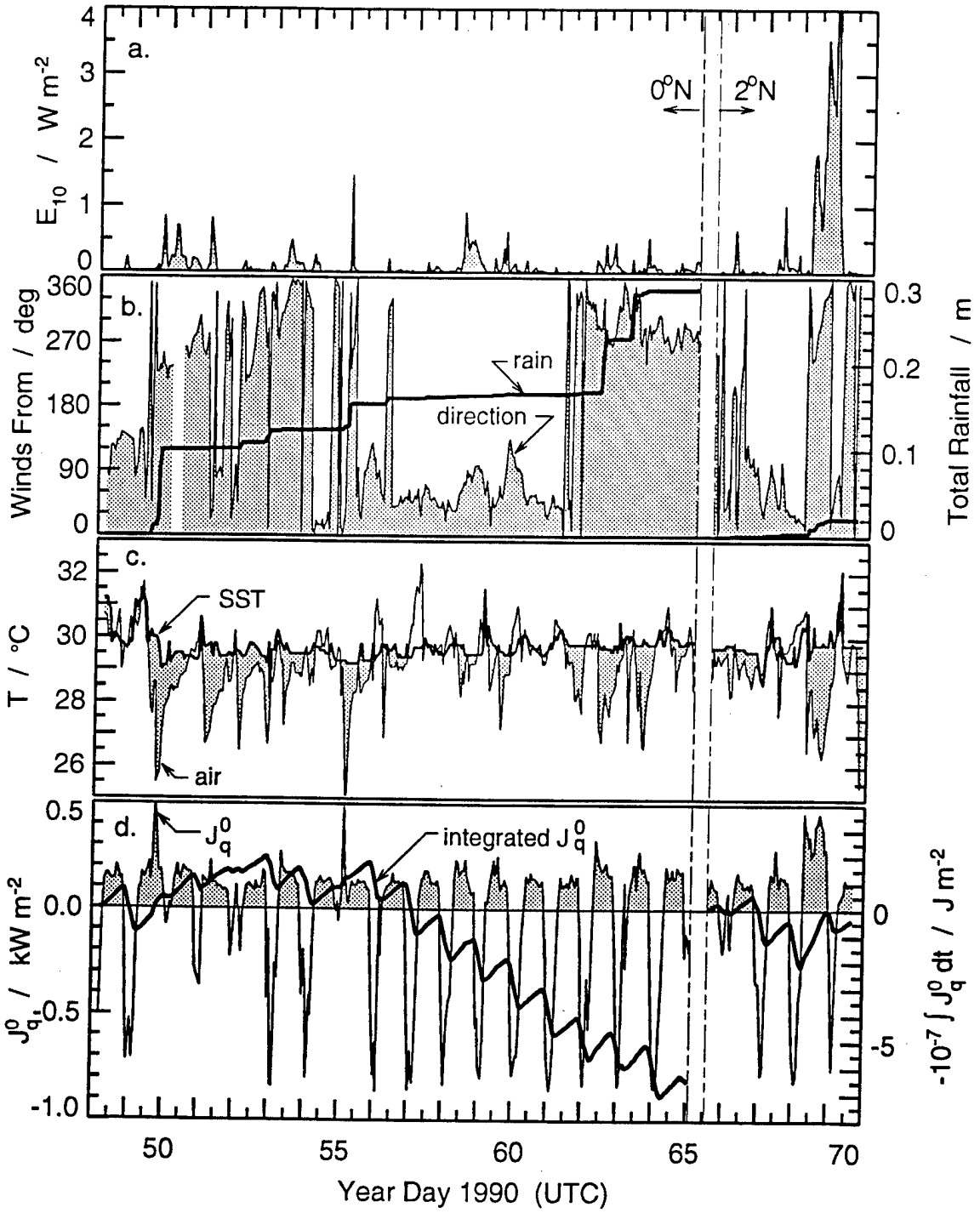
a.
0°N
2°N
E_{10} / W m^{-2}
b.
rain
direction
Winds From / deg
Total Rainfall / m
c.
SST
air
T / °C
d.
J_q^0
integrated J_q^0
J_q^0 / kW m^{-2}
-10^{-7} ∫ J_q^0 dt / J m^{-2}
Year Day 1990 (UTC)

Fig. 1

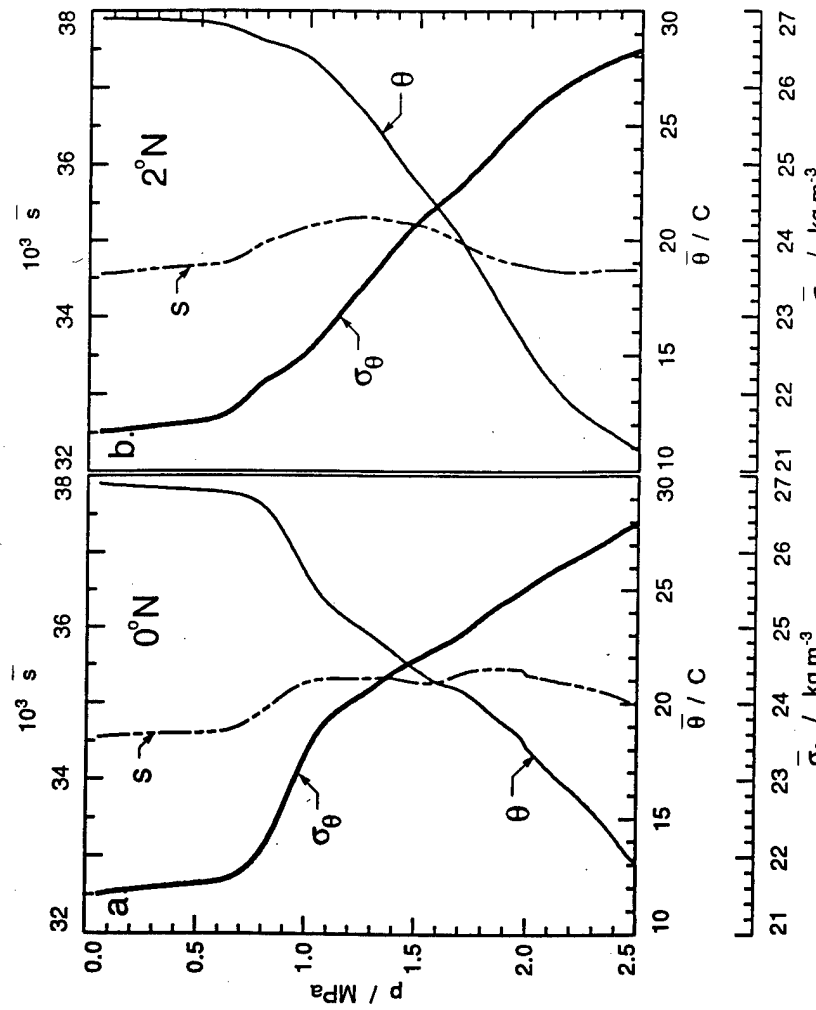

FIG. 2

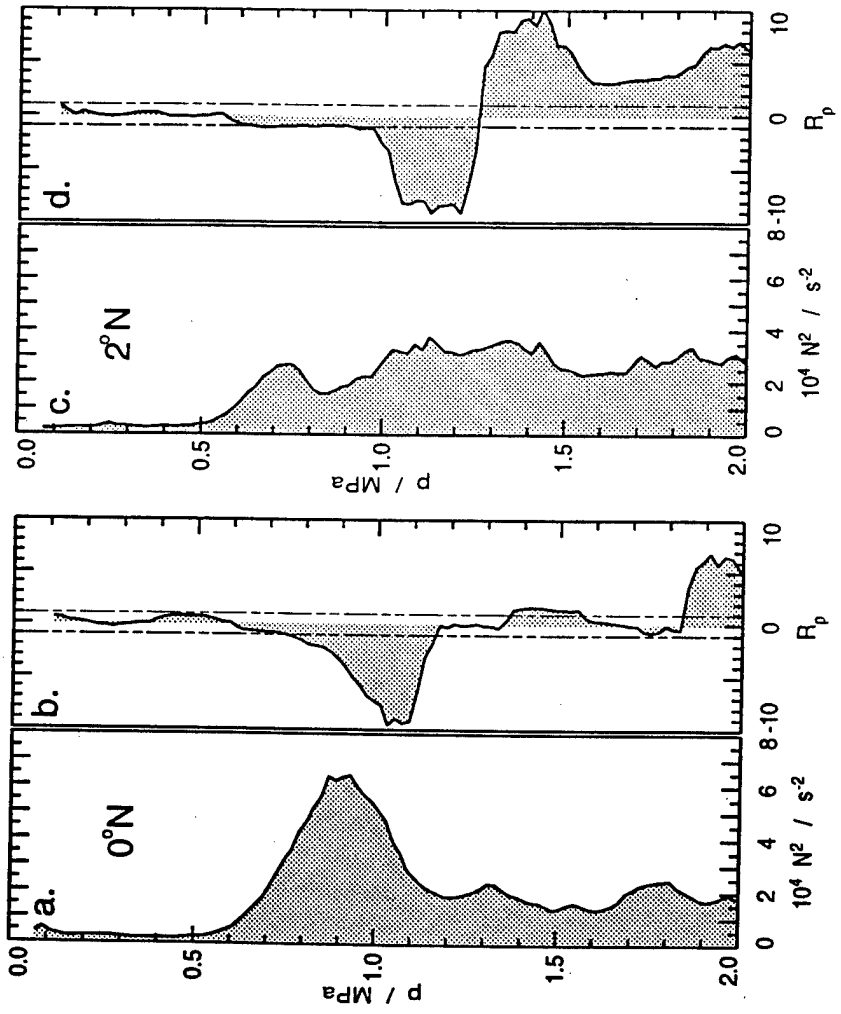

FIG. 3

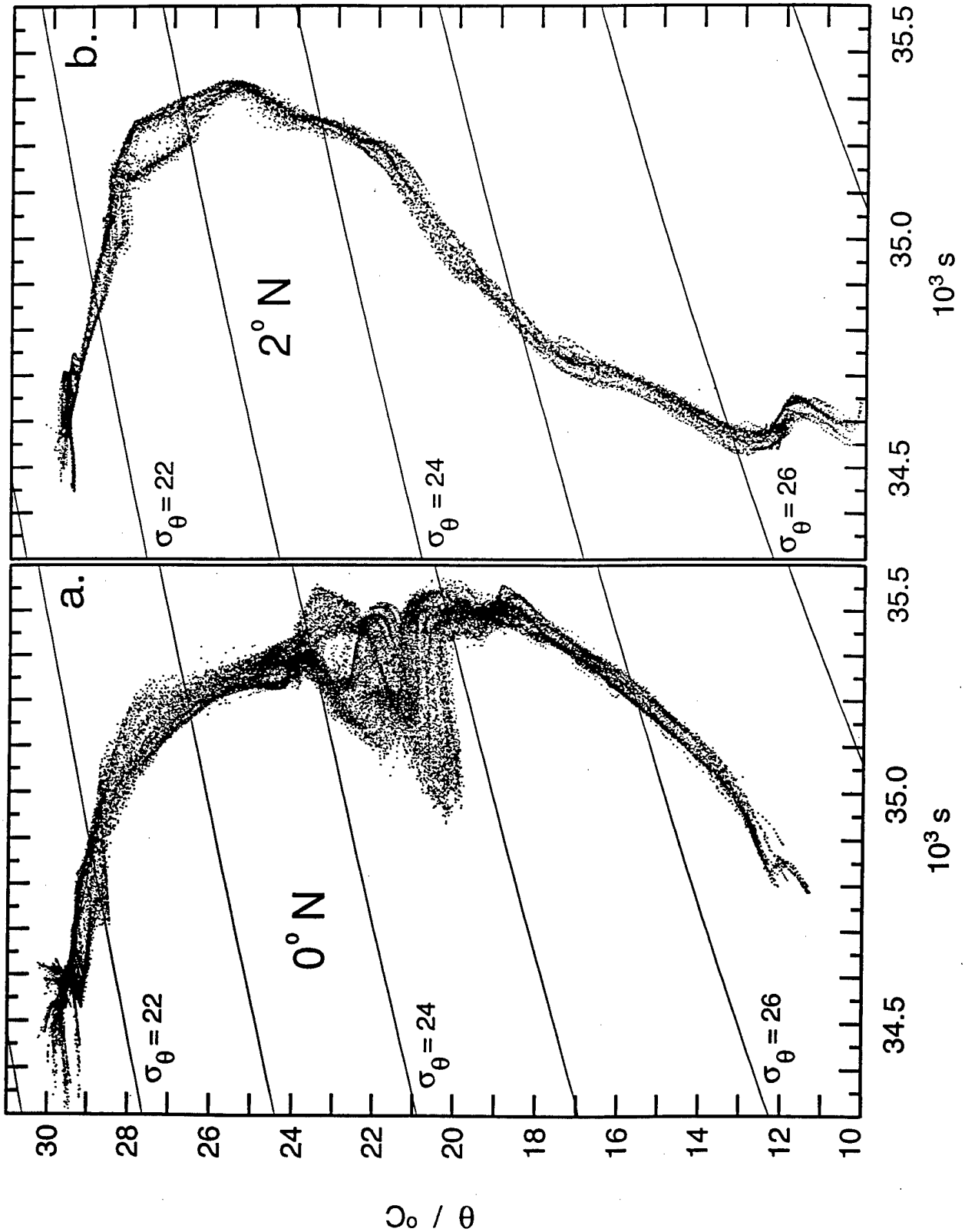
a.
b.
0° N
2° N
σθ = 22
σθ = 24
σθ = 26
θ / °C
10³ s
34.5
35.0
35.5
10
12
14
16
18
20
22
24
26
28
30

FIG. 4

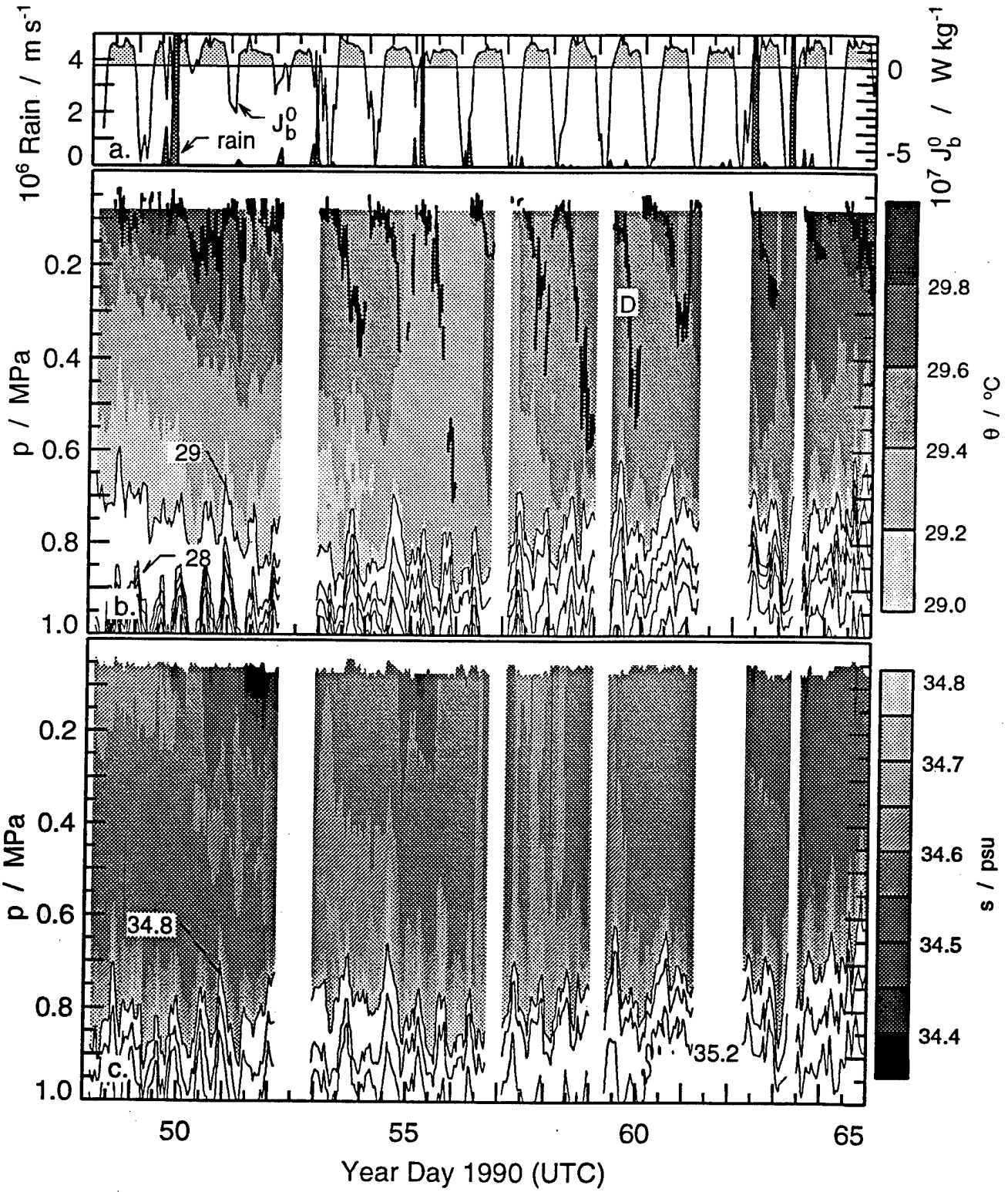
10^6 Rain / m s^-1
4
2
0
a.
rain
J_b^0
0
-5
10^7 J_b^0 / W kg^-1
p / MPa
0.2
0.4
0.6
0.8
1.0
29
28
b.
D
29.8
29.6
29.4
29.2
29.0
θ / °C
34.8
c.
35.2
34.8
34.7
34.6
34.5
34.4
s / psu
50
55
60
65
Year Day 1990 (UTC)

FIG. 5

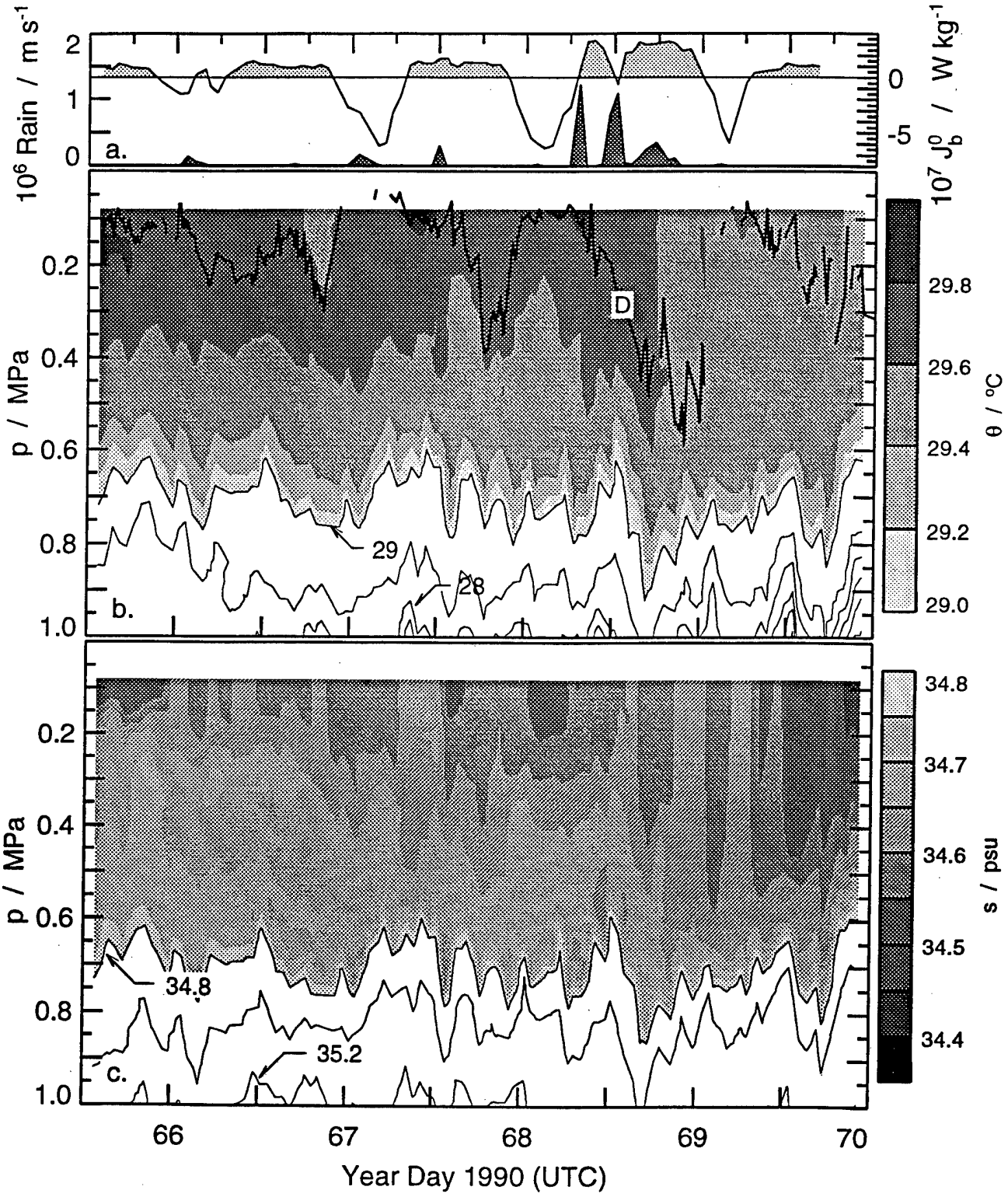
10^6 Rain / m s^-1
2
1
0
a.
10^7 J_b^0 / W kg^-1
0
-5
p / MPa
0.2
0.4
0.6
0.8
1.0
D
29
28
b.
θ / °C
29.8
29.6
29.4
29.2
29.0
p / MPa
0.2
0.4
0.6
0.8
1.0
34.8
35.2
c.
s / psu
34.8
34.7
34.6
34.5
34.4
66
67
68
69
70
Year Day 1990 (UTC)

Fig. 6

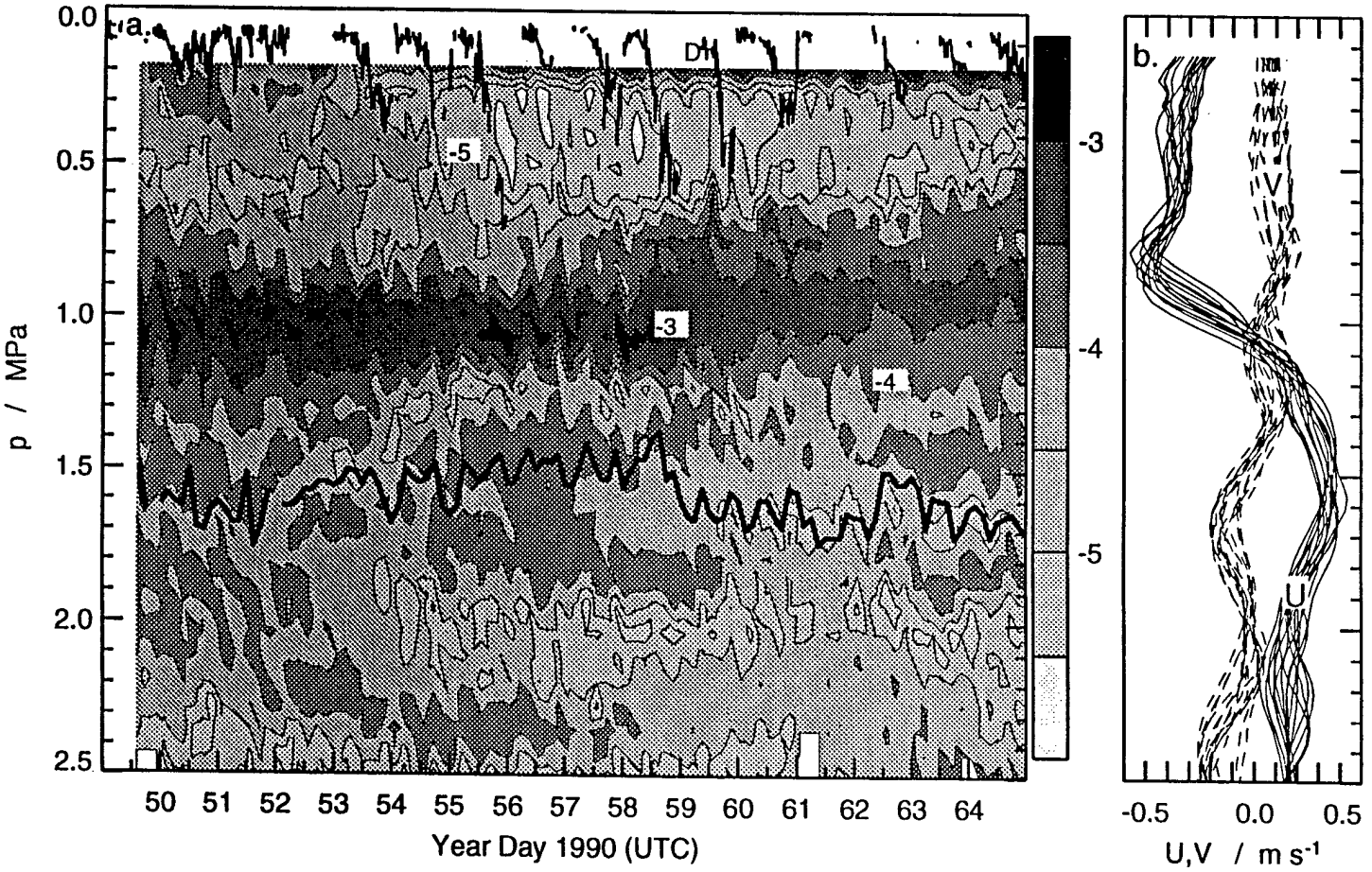
a.
b.
DH
-5
-3
-4
0.0
0.5
1.0
1.5
2.0
2.5
p / MPa
50 51 52 53 54 55 56 57 58 59 60 61 62 63 64
Year Day 1990 (UTC)
-3
-4
-5
V
U
-0.5
0.0
0.5
U,V / m s-1

Fig. 7

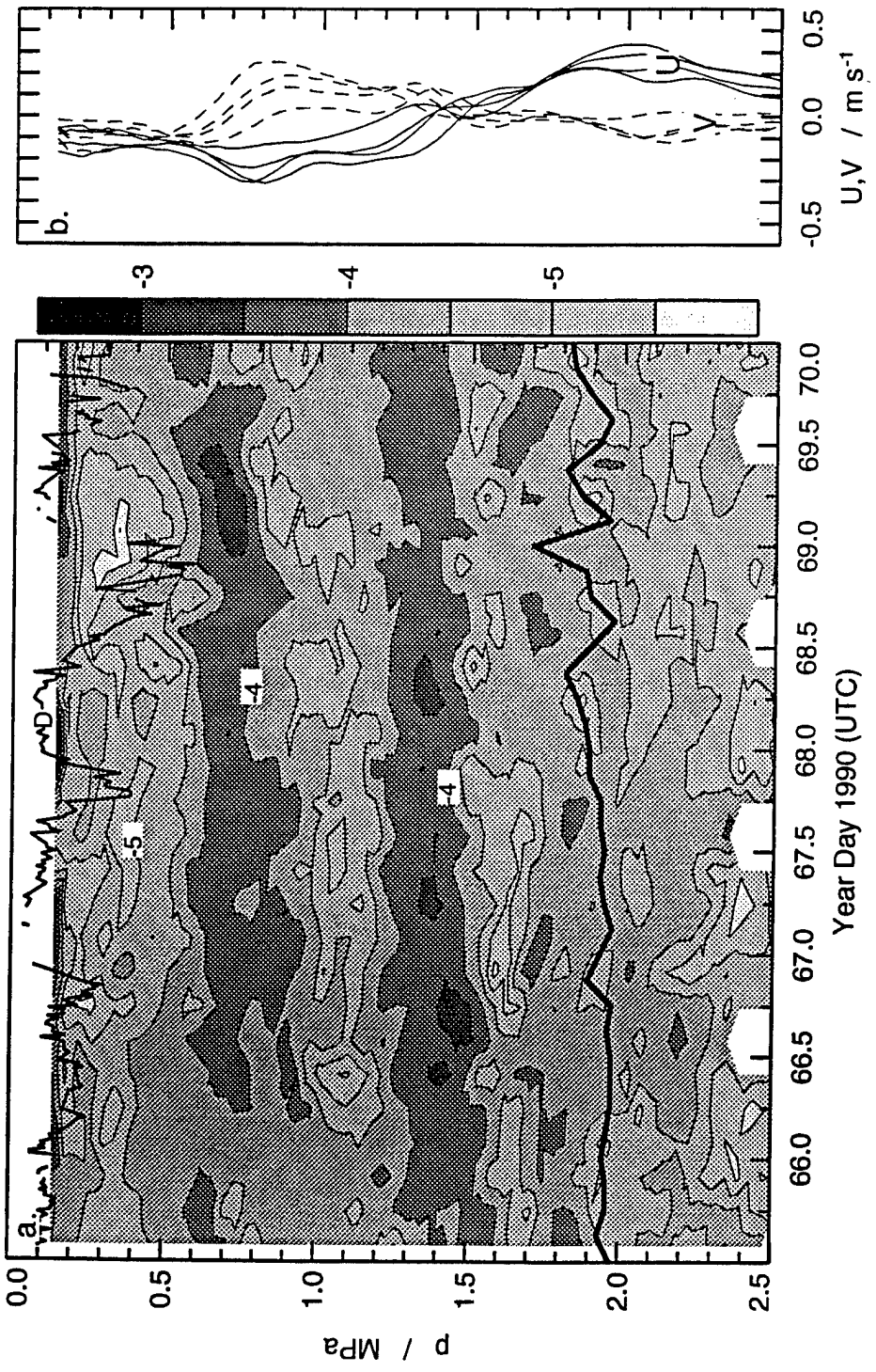
a.
b.
-3
-4
-5
-4
-5
-4
0.0
0.5
1.0
1.5
2.0
2.5
p / MPa
66.0
66.5
67.0
67.5
68.0
68.5
69.0
69.5
70.0
Year Day 1990 (UTC)
-0.5
0.0
0.5
U,V / m s-1
U
V

FIG. 8

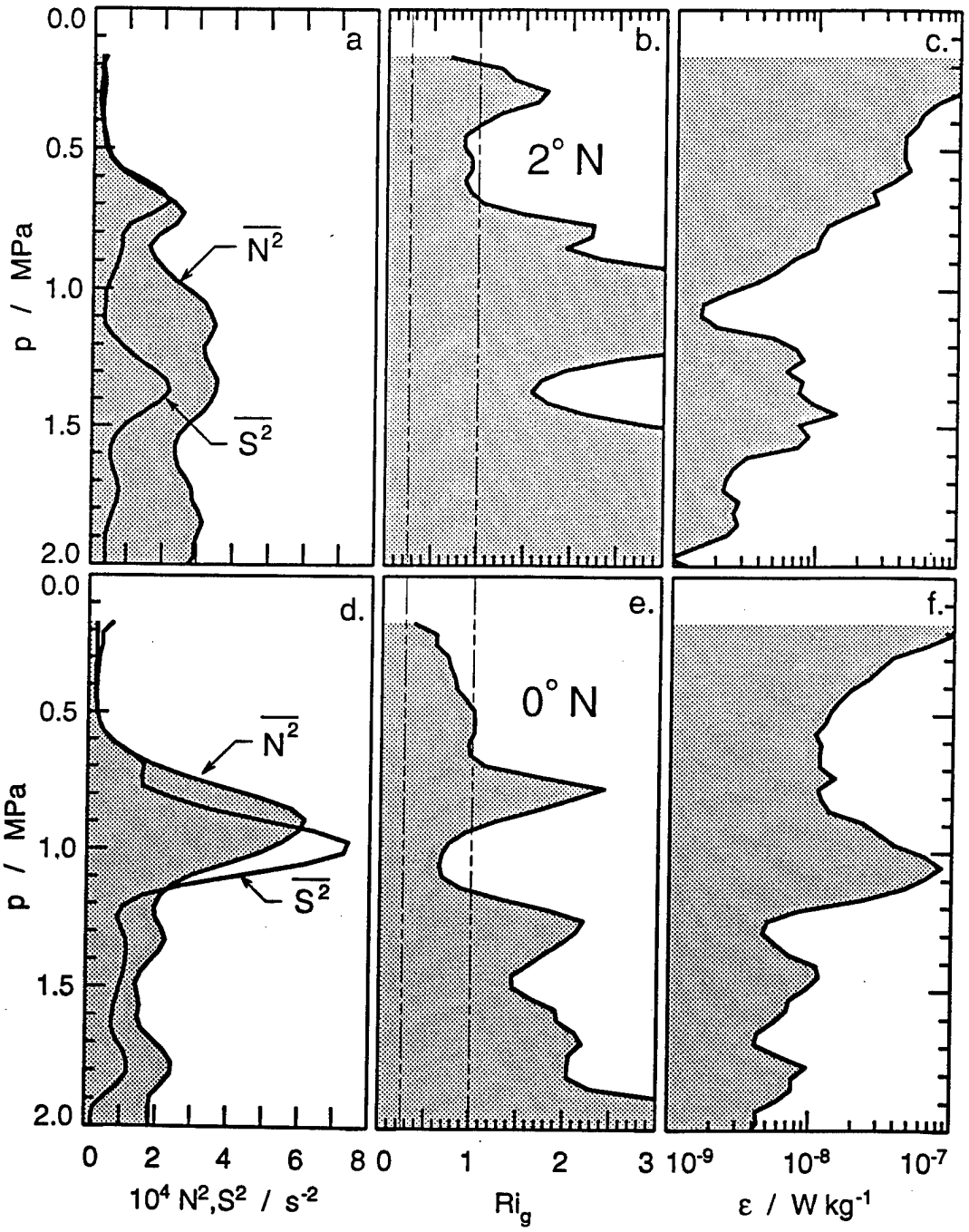
a
b.
c.
d.
e.
f.
2° N
0° N
$\overline{N^2}$
$\overline{S^2}$
p / MPa
0.0
0.5
1.0
1.5
2.0
0 2 4 6 8
10^4 N^2,S^2 / s^{-2}
0 1 2 3
Ri_g
10^{-9} 10^{-8} 10^{-7}
ε / W kg^{-1}

Fig. 9

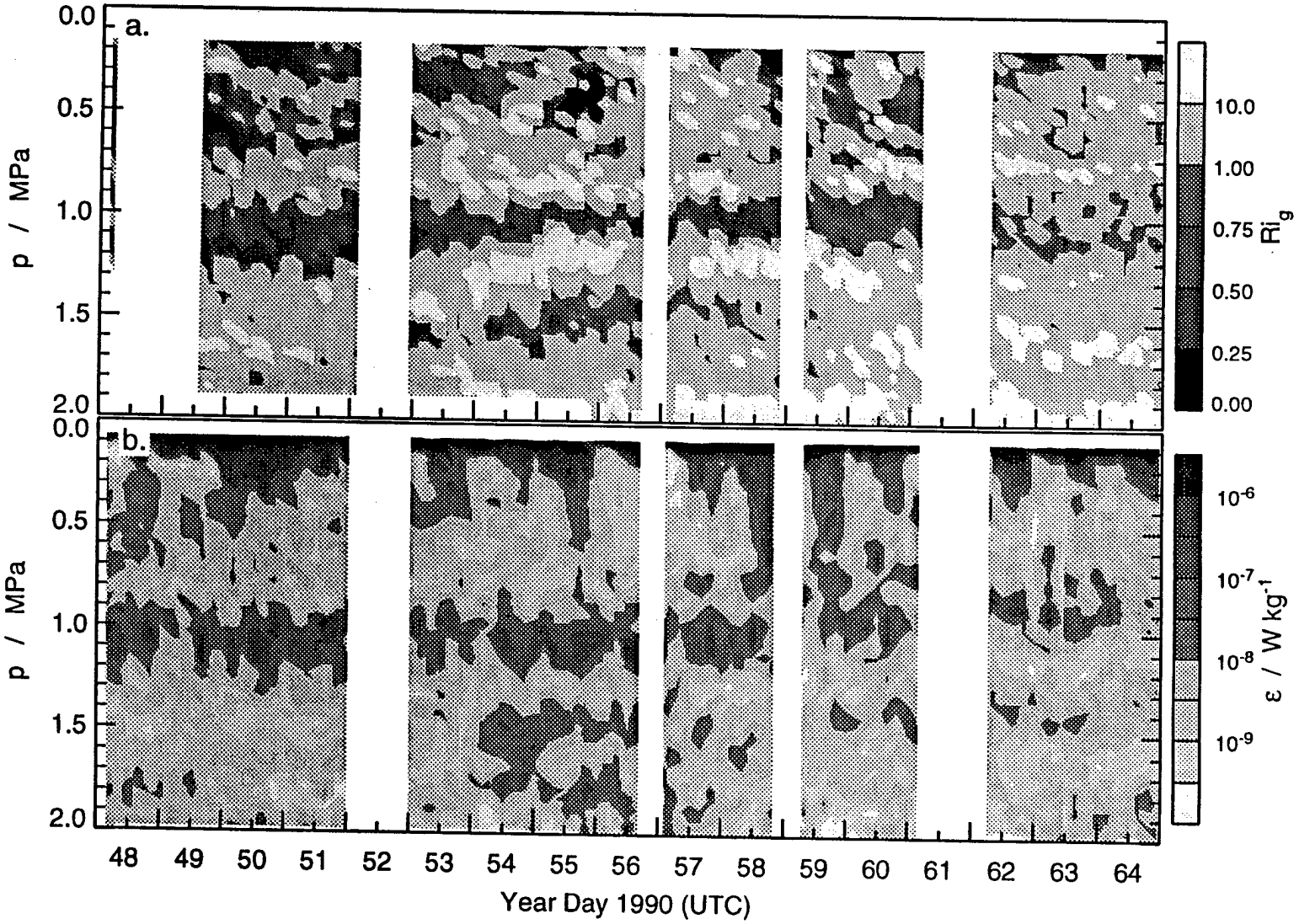
a.
b.
0.0
0.5
1.0
1.5
2.0
p / MPa
10.0
1.00
0.75
0.50
0.25
0.00
Ri_g
10^-6
10^-7
10^-8
10^-9
ε / W kg^-1
48
49
50
51
52
53
54
55
56
57
58
59
60
61
62
63
64
Year Day 1990 (UTC)

Fig. 10

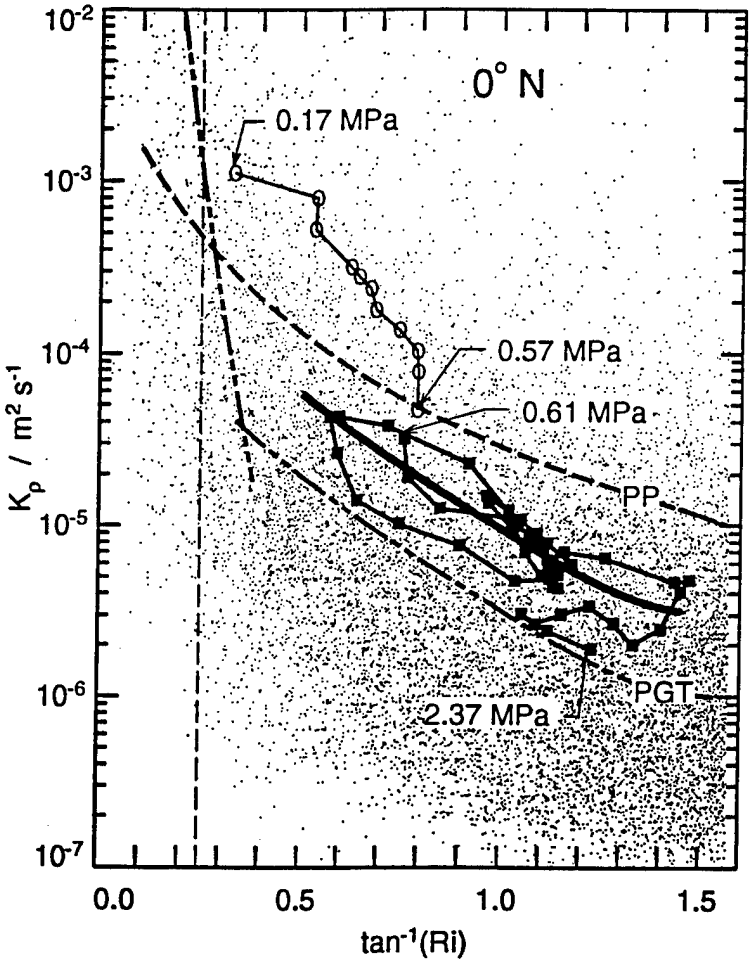
0° N
0.17 MPa
0.57 MPa
0.61 MPa
PP
PGT
2.37 MPa
10^{-2}
10^{-3}
10^{-4}
10^{-5}
10^{-6}
10^{-7}
K_ρ / $m^2 s^{-1}$
0.0
0.5
1.0
1.5
$\tan^{-1}$(Ri)

Fig. 11

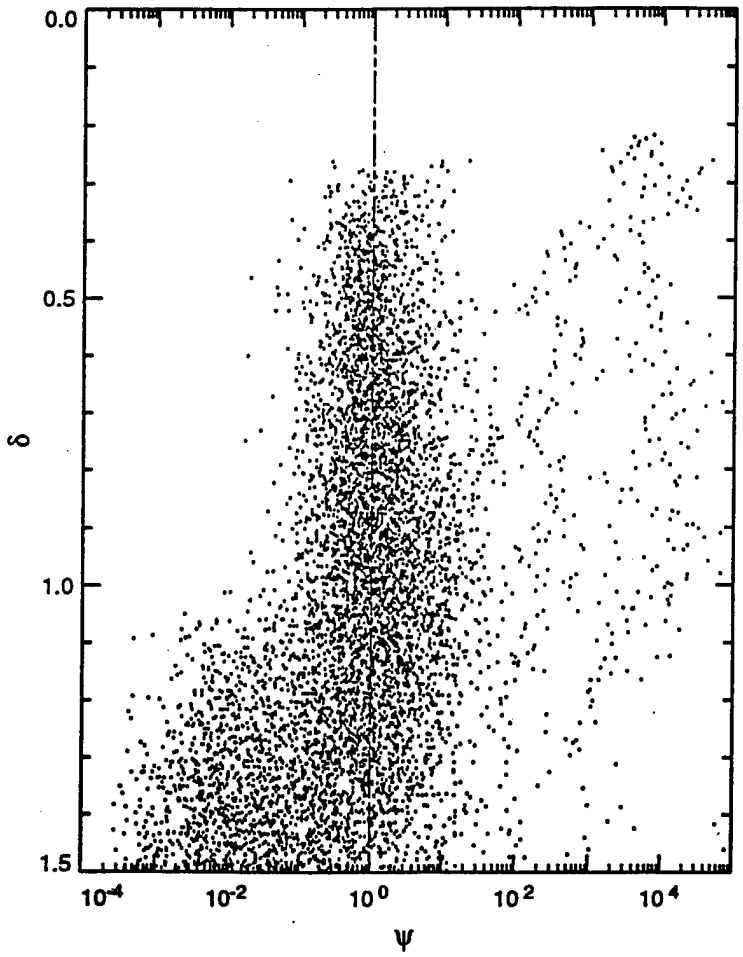

FIG. 12

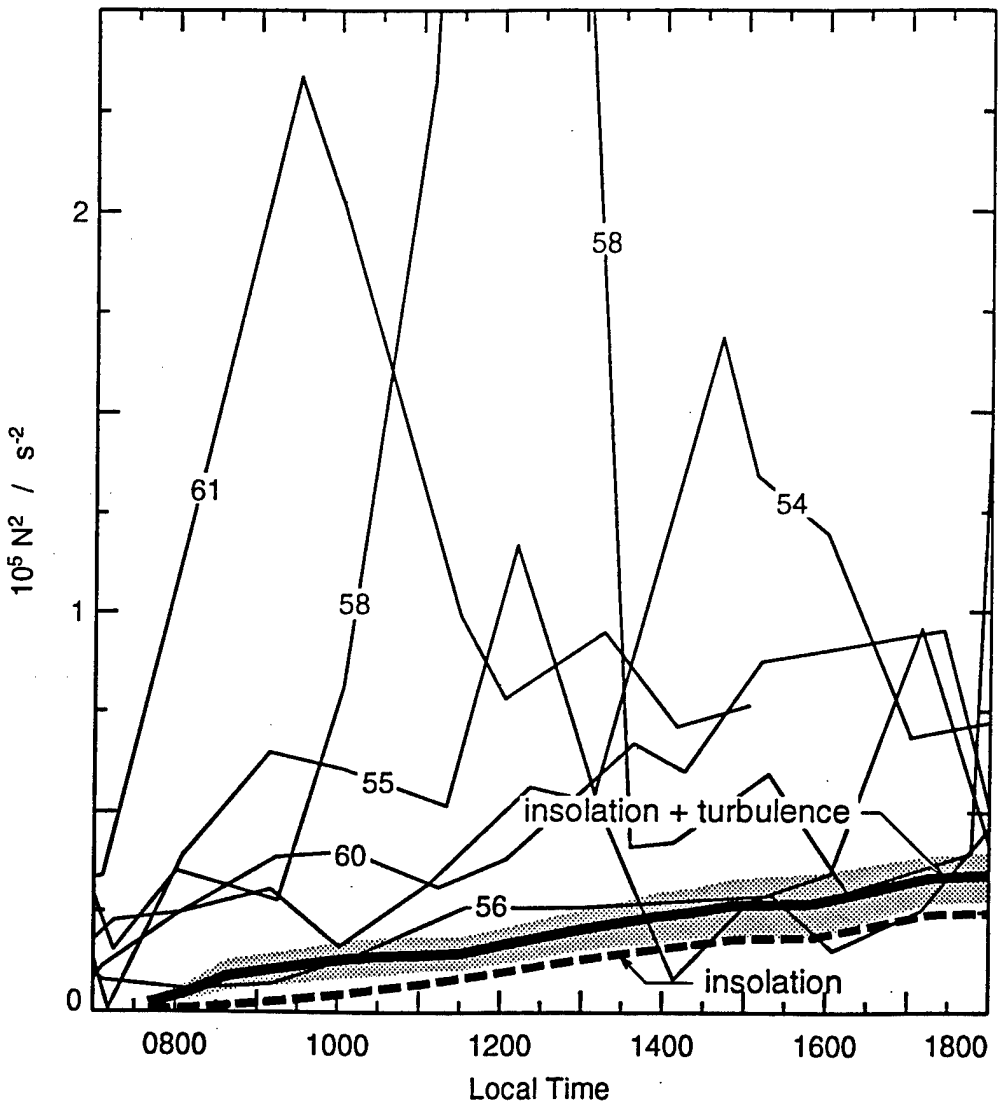
2
1
0
10^5 N^2 / s^{-2}
61
58
58
54
55
insolation + turbulence
60
56
insolation
0800
1000
1200
1400
1600
1800
Local Time

Fig. 13

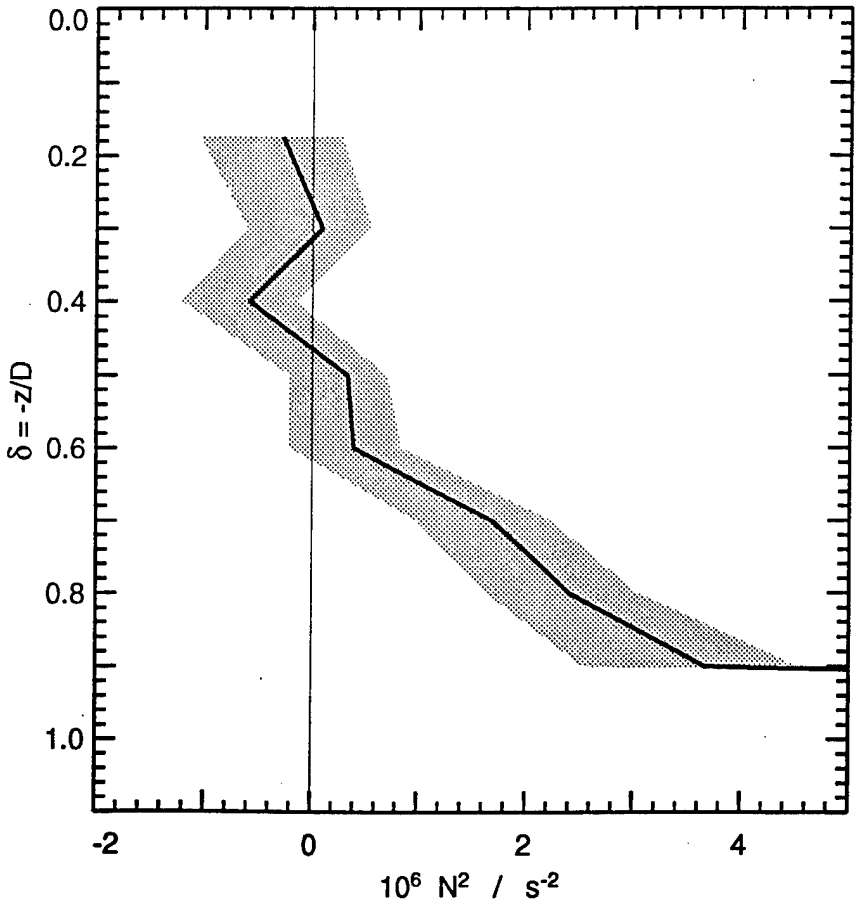

Fig. 14

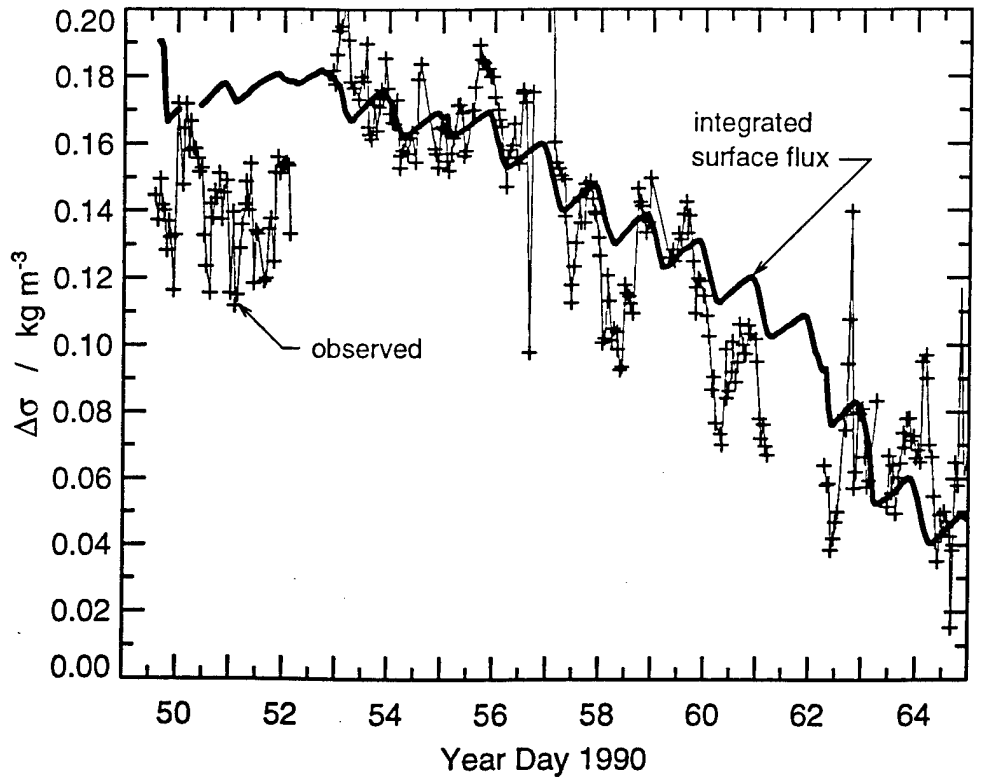
0.20
0.18
0.16
0.14
0.12
0.10
0.08
0.06
0.04
0.02
0.00
Δσ / kg m-3
integrated
surface flux
observed
50
52
54
56
58
60
62
64
Year Day 1990

FIG. 15

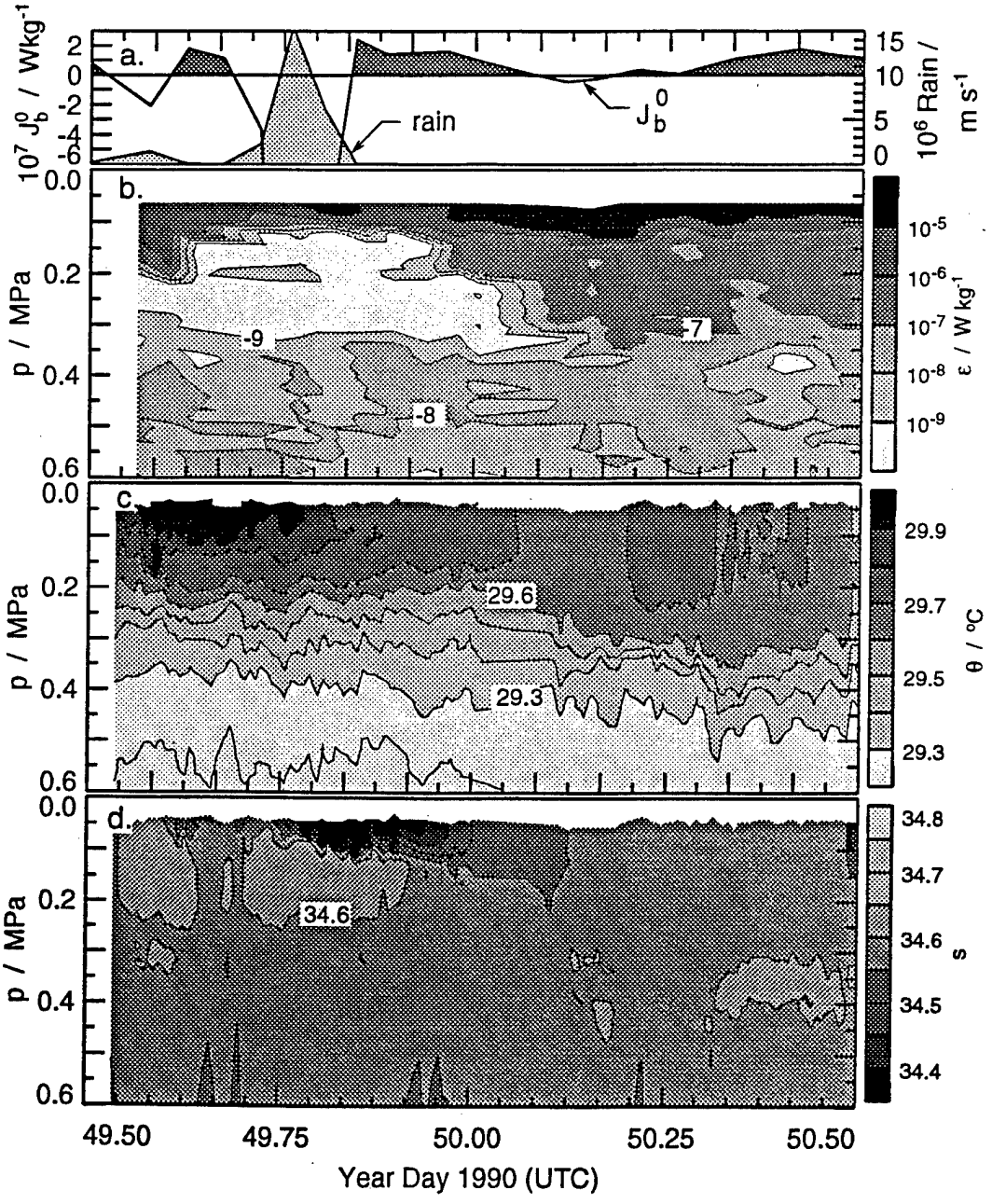
a.
b.
c.
d.
rain
J_b^0
10^7 J_b^0 / Wkg^{-1}
10^6 Rain / m s^{-1}
p / MPa
-9
-8
-7
29.6
29.3
34.6
10^{-5}
10^{-6}
10^{-7}
10^{-8}
10^{-9}
ε / W kg^{-1}
θ / °C
s
49.50
49.75
50.00
50.25
50.50
Year Day 1990 (UTC)

FIG. 16

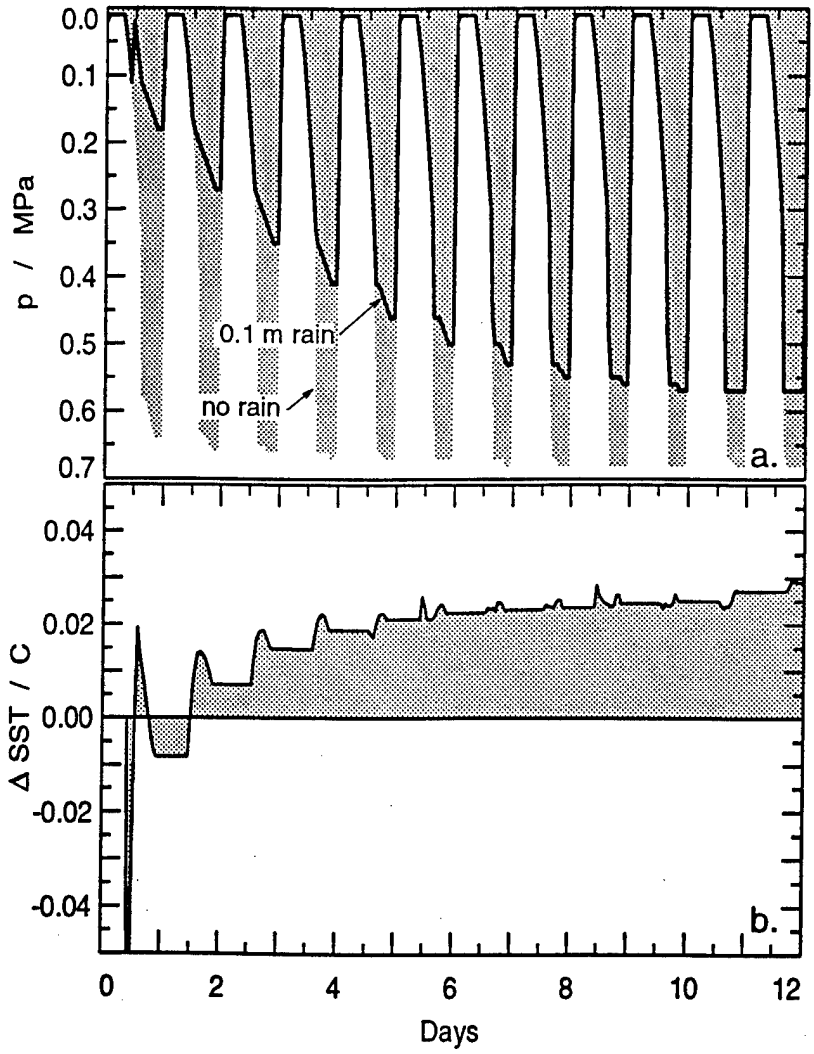
0.0
0.1
0.2
0.3
0.4
0.5
0.6
0.7
p / MPa
0.1 m rain
no rain
a.
0.04
0.02
0.00
-0.02
-0.04
Δ SST / C
b.
0
2
4
6
8
10
12
Days

FIG. 17

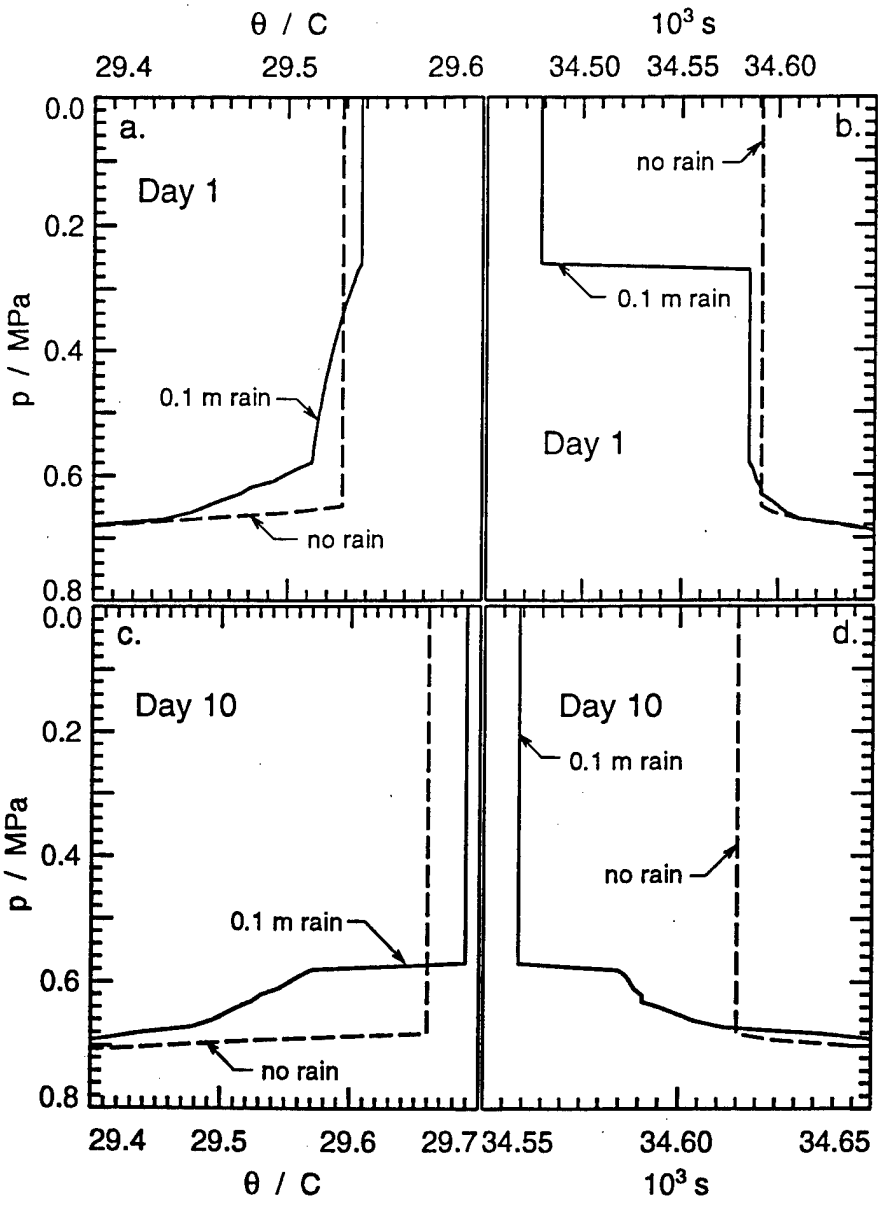
θ / C
10³ s
29.4
29.5
29.6
34.50
34.55
34.60
a.
b.
c.
d.
Day 1
Day 1
Day 10
Day 10
0.1 m rain
no rain
0.1 m rain
no rain
0.1 m rain
no rain
0.1 m rain
no rain
p / MPa
0.0
0.2
0.4
0.6
0.8
29.4
29.5
29.6
29.7
34.55
34.60
34.65
θ / C
10³ s

Fig. 1B

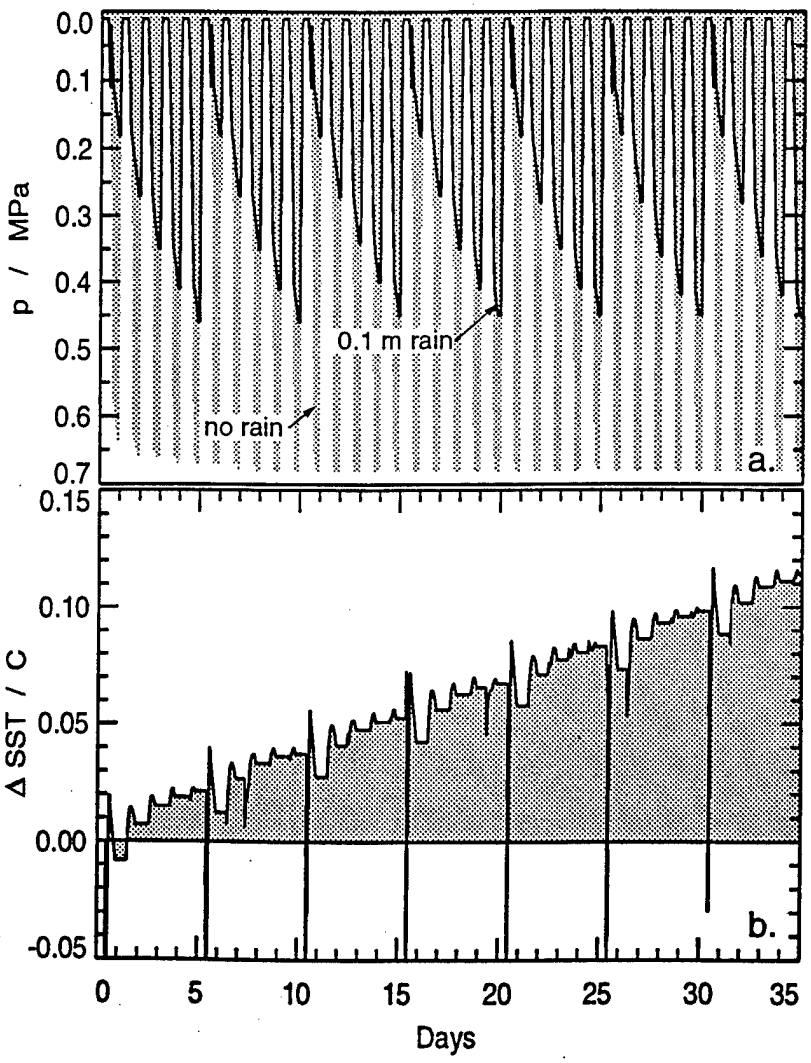
0.0
0.1
0.2
0.3
0.4
0.5
0.6
0.7
p / MPa
0.1 m rain
no rain
a.
0.15
0.10
0.05
0.00
-0.05
Δ SST / C
b.
0
5
10
15
20
25
30
35
Days

Fig. 19

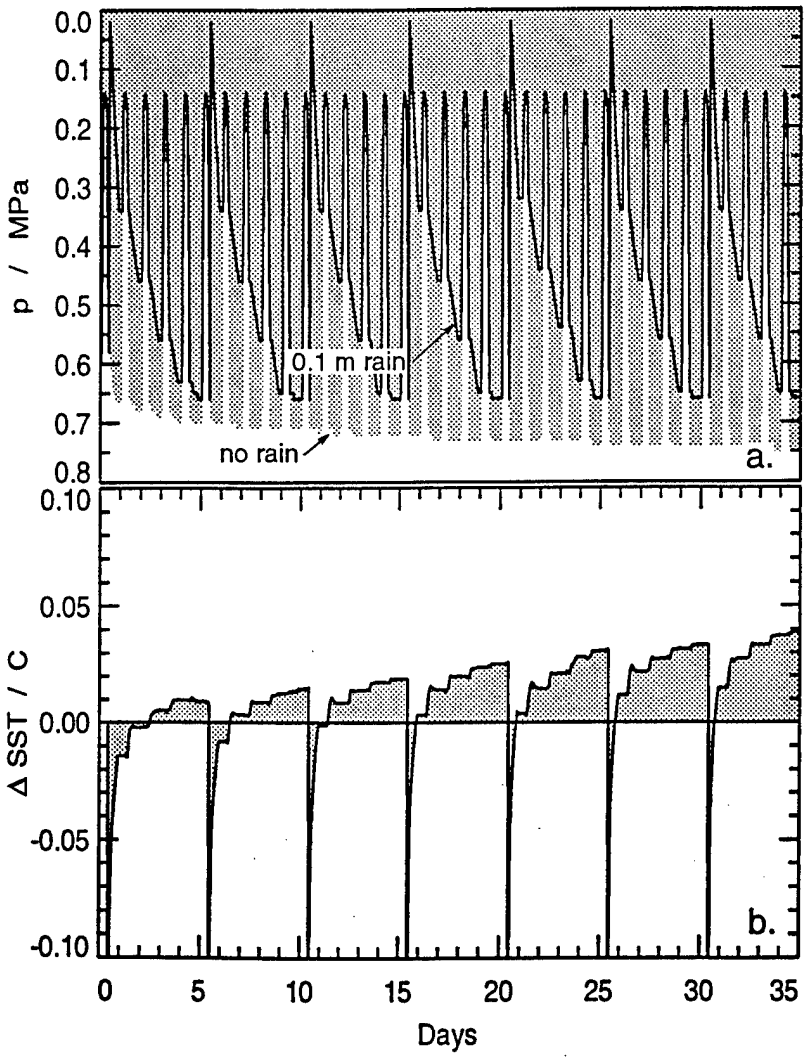
0.0
0.1
0.2
0.3
0.4
0.5
0.6
0.7
0.8
p / MPa
0.1 m rain
no rain
a.
0.10
0.05
0.00
-0.05
-0.10
Δ SST / C
b.
0
5
10
15
20
25
30
35
Days

FIG. 20

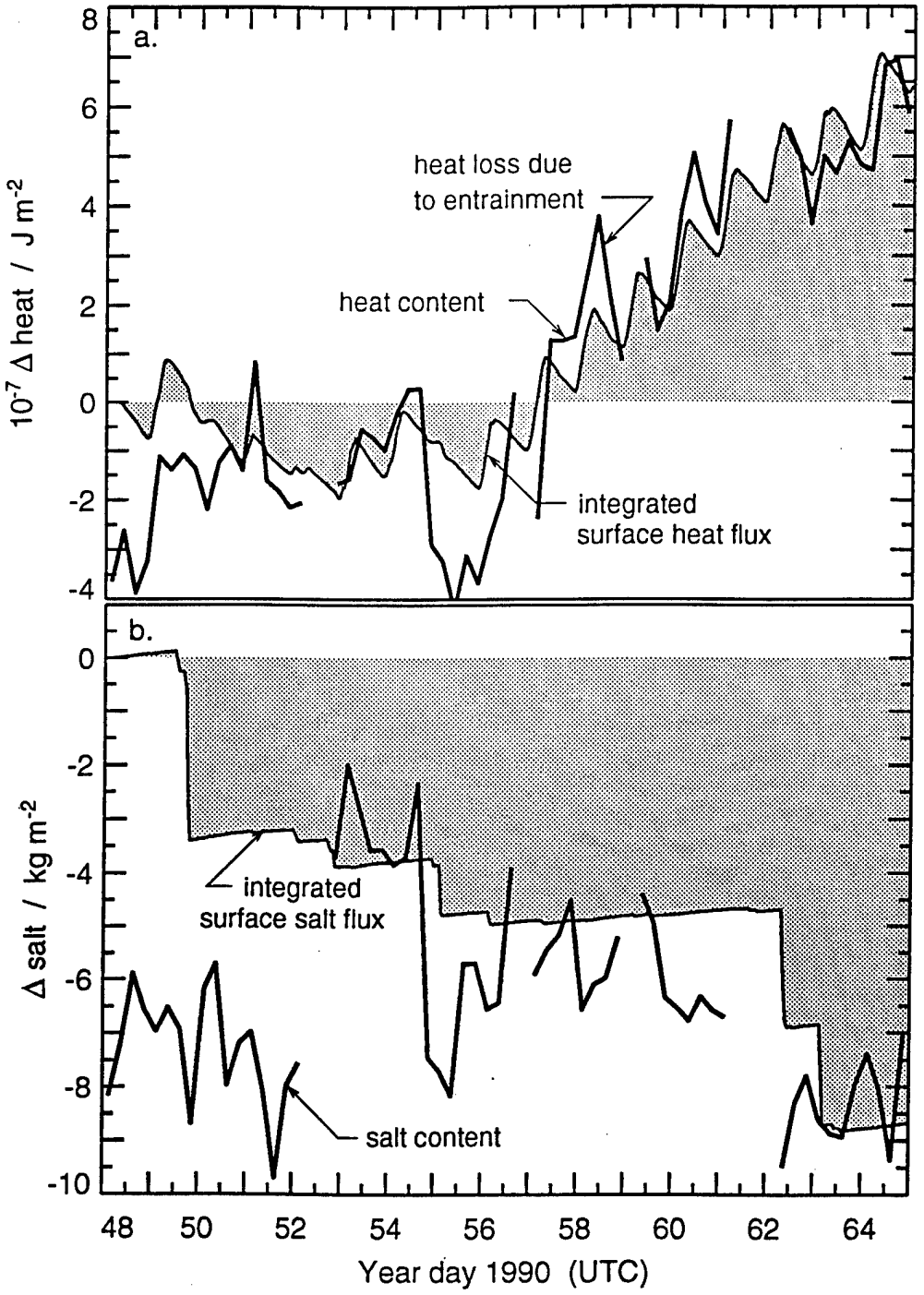
a.
b.
heat loss due
to entrainment
heat content
integrated
surface heat flux
integrated
surface salt flux
salt content
10^{-7} Δ heat / J m^{-2}
Δ salt / kg m^{-2}
Year day 1990 (UTC)
8
6
4
2
0
-2
-4
-6
-8
-10
48
50
52
54
56
58
60
62
64

FIG. 21

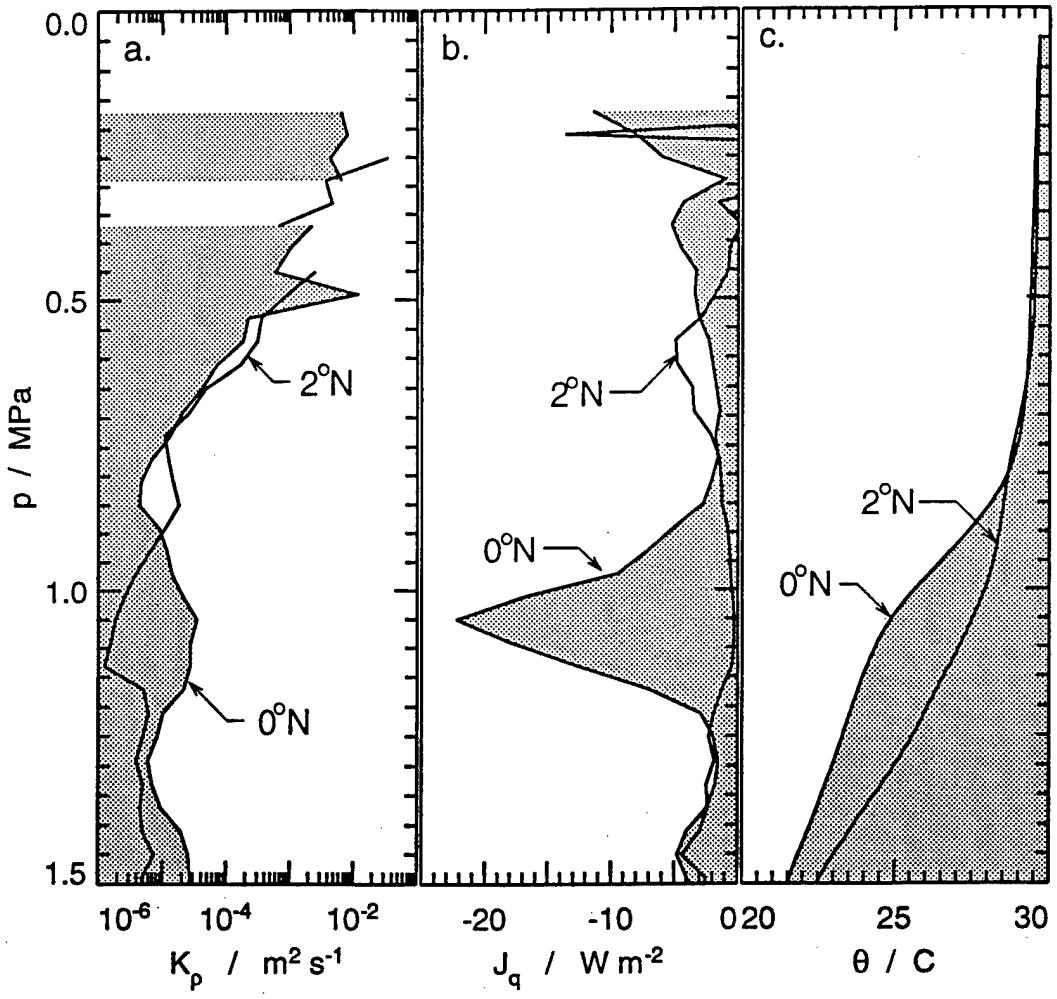
a.
b.
c.
0.0
0.5
1.0
1.5
p / MPa
2°N
0°N
2°N
0°N
2°N
0°N
10-6
10-4
10-2
Kρ / m2 s-1
-20
-10
0
20
Jq / W m-2
25
30
θ / C

Fig. 22

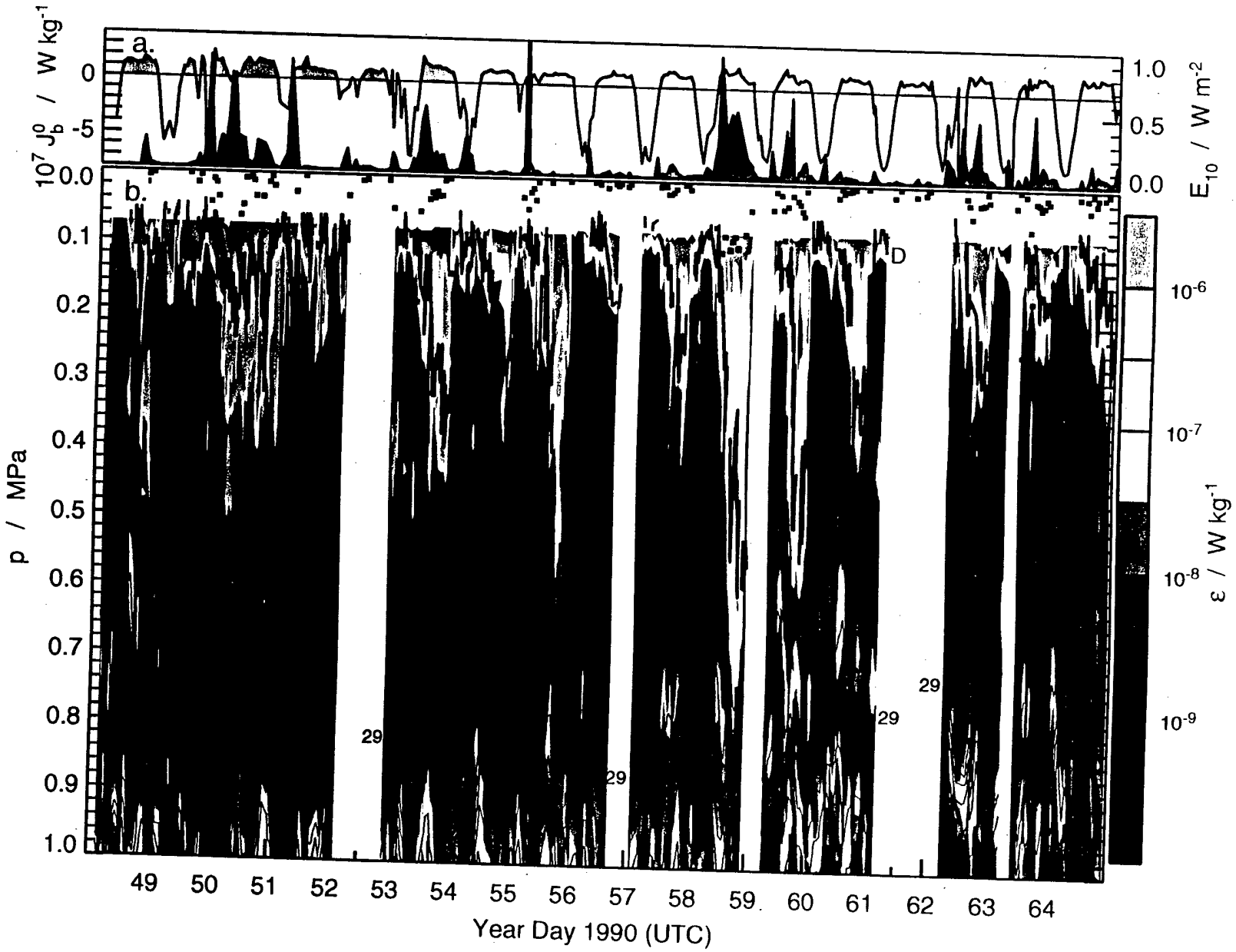
a.
b.
10^7 J_b^0 / W kg^{-1}
0
-5
0.0
1.0
0.5
0.0
E_{10} / W m^{-2}
p / MPa
0.1
0.2
0.3
0.4
0.5
0.6
0.7
0.8
0.9
1.0
D
29
29
29
29
10^{-6}
10^{-7}
10^{-8}
10^{-9}
ε / W kg^{-1}
49
50
51
52
53
54
55
56
57
58
59
60
61
62
63
64
Year Day 1990 (UTC)

Fig. 23

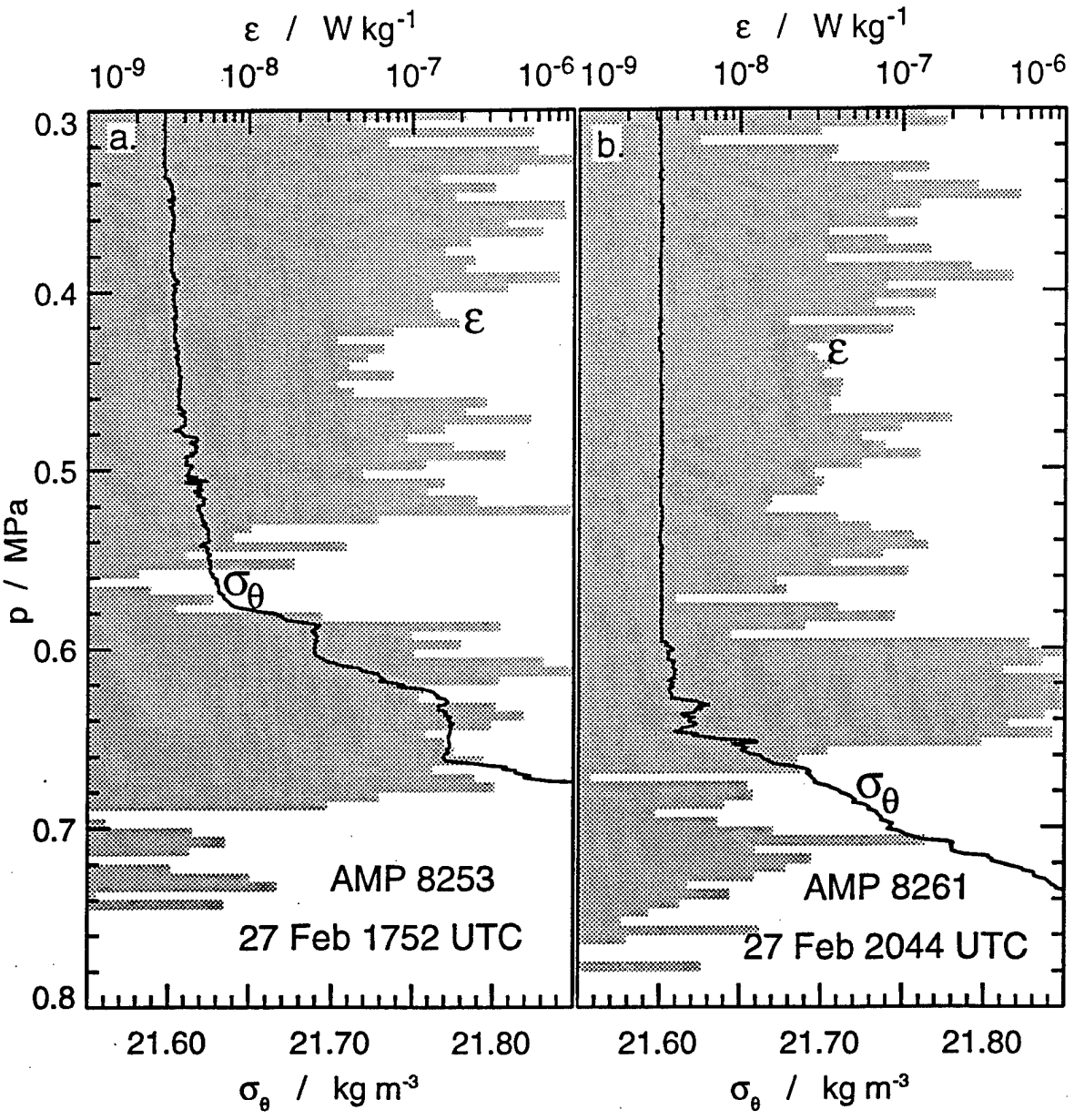
ε / W kg-1
10-9
10-8
10-7
10-6
a.
b.
ε
σθ
p / MPa
0.3
0.4
0.5
0.6
0.7
0.8
AMP 8253
27 Feb 1752 UTC
AMP 8261
27 Feb 2044 UTC
21.60
21.70
21.80
σθ / kg m-3

FIG. 24

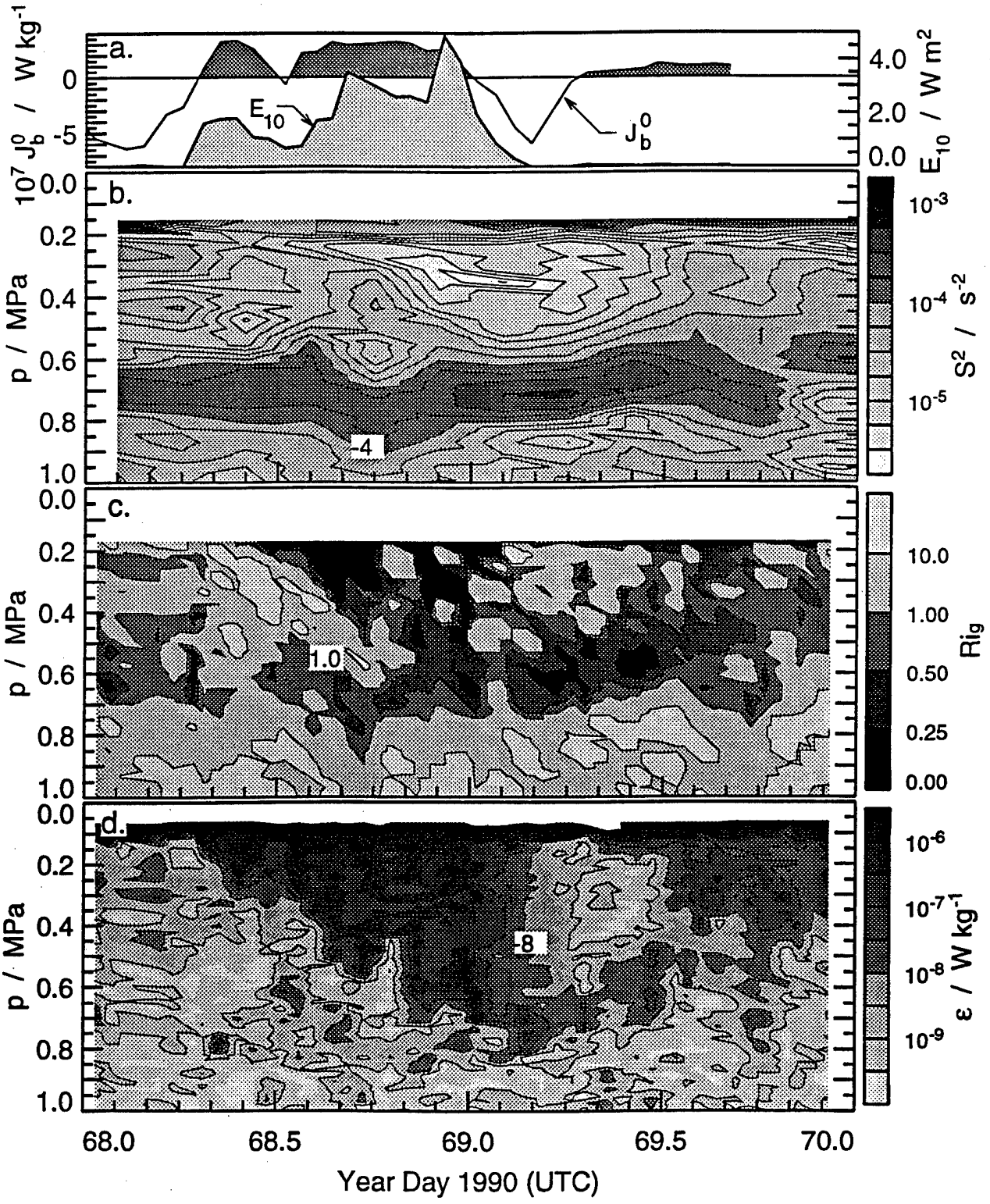
a.
b.
c.
d.
$10^7 J_b^0$ / W kg^{-1}
E_{10}
J_b^0
E_{10} / W m^2
p / MPa
S^2 / s^{-2}
Ri$_g$
ε / W kg^{-1}
-4
1.0
-8
Year Day 1990 (UTC)

Fig. 25

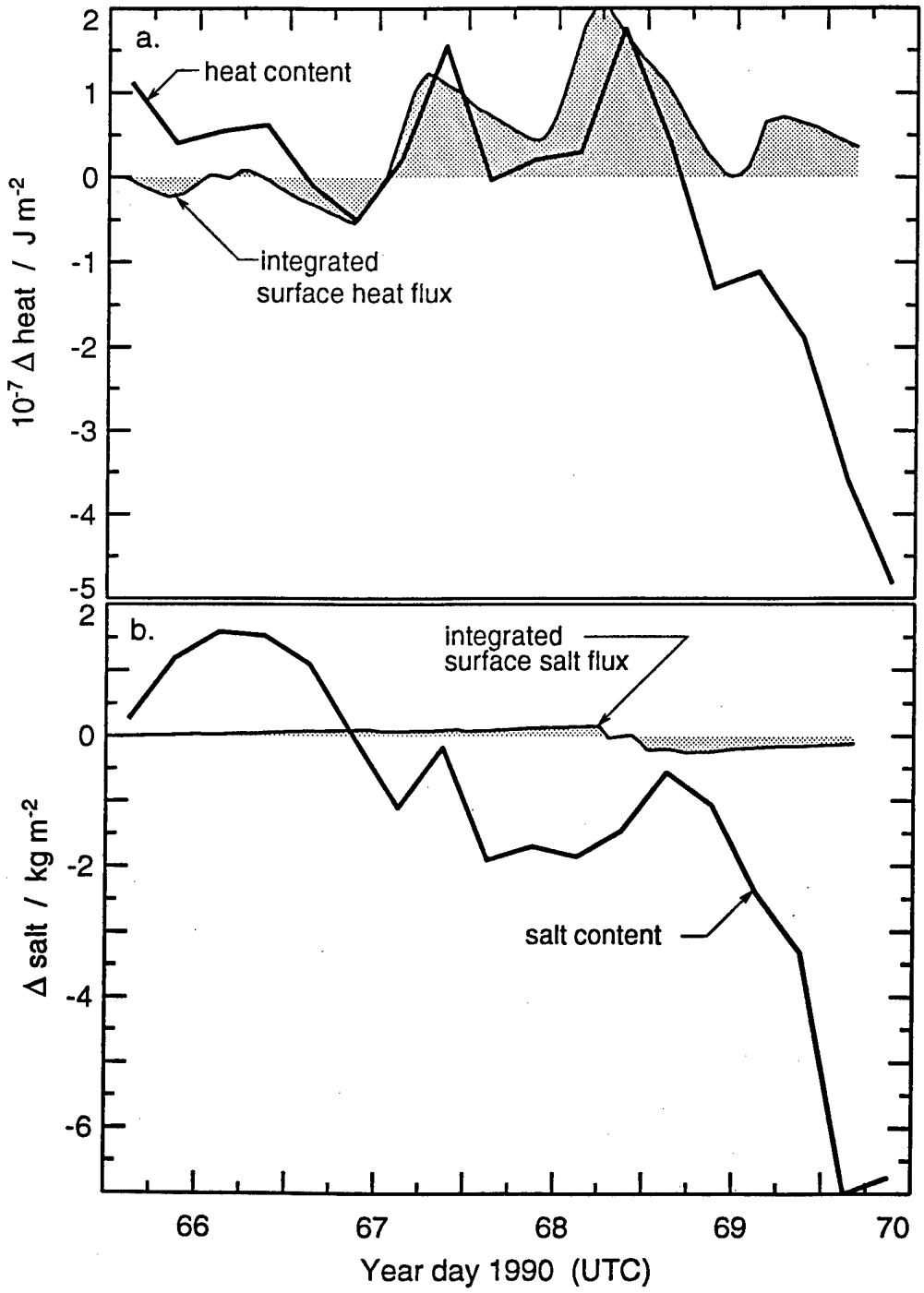
a.
heat content
integrated
surface heat flux
10^{-7} Δ heat / J m^{-2}
2
1
0
-1
-2
-3
-4
-5
b.
integrated
surface salt flux
salt content
Δ salt / kg m^{-2}
2
0
-2
-4
-6
66
67
68
69
70
Year day 1990 (UTC)

Fig. 26